

ABSTRACT

TAN, BIKAN. First-Principles Studies of Conformation and Solution Effects on DNA Transport. (Under the direction of Dr. Jerry Bernholc.)

DNA charge transport (CT) has attracted considerable attention by the scientific community over the past 20 years. This interest reflects the potential of DNA CT to provide a sensitive route for signaling, whether in the construction of a nano-scale biosensor or as an enzymatic tool to detect damage in the genome. Research in DNA CT began as a quest to determine whether the DNA double helix with π -stacked base pairs might share the conductive characteristics of π -stacked solids. Physicists carried out sophisticated experiments to measure the conductivity of DNA. But the means to connect DNA to the electrodes, as well as the conditions under which the conductivity was measured are different among many experiments, as the results of the current measurements. DNA CT was seen to depend upon the connection between electrodes and DNA, and coupling between the DNA base pair stacks. Importantly, for those studies that utilized well-characterized connections to the DNA and preserved the duplex native conformation in buffered solution, significant electron conductivities were achieved. Certainly, the debate among researches has shifted from "Is DNA CT possible?" to "How does it work?".

To investigate the remarkable characteristics of the double-helix molecule, we use a first-principle technique combined with molecular dynamics simulations to calculate the transport properties of B-DNA sandwiched between carbon nanotubes via alkane linkers. The quantum results using the NEGF method are calculated from snapshots recorded in MD trajectories. In chapter 1, we will go through the basic quantum and classic theories on which our calculations are based. The subject of DNA structure, electronic properties and its potential application in many fields will be introduced in chapter 2. In chapter

3, we discuss our results towards the understanding of the mechanism of DNA charge transport.

© Copyright 2014 by Bikan Tan
All Rights Reserved

First-Principles Studies of Conformation and Solution Effects on DNA Transport

by
Bikan Tan

A dissertation submitted to the Graduate Faculty of
North Carolina State University
in partial fulfillment of the
requirements for the Degree of
Doctor of Philosophy

Physics

Raleigh, North Carolina

2014

APPROVED BY:

Dr. Miroslav Hodak

Dr. Wenchang Lu

Dr. Zhilin Li

Dr. Jerry Bernholc
Chair of Advisory Committee

DEDICATION

To my loving son, my wife, my parents and my friends.

BIOGRAPHY

The author was born on December 9th, 1983 in Changsha, Hunan Province, China. He graduated from Yali Middle school in Changsha in the year of 2002. He started his undergraduate education at Nanjing Univeristy in Nanjing, China, and received his Bachelor of Sciences degree in theoretical physics in 2006. He then was admitted as as a graduate student in the Department of Physics in Nanjing University with a honored waiver of entrance test. To pursue higher level academic goals, he decided to come to United States, joined the Ph.D program in the Department of Physics at North Carolina State University in August 2007 and passed the Ph.D written qualification exam in January 2008. In the summer of 2008, he joined Dr. Bernholc's group to explore high level computational physics.

ACKNOWLEDGEMENTS

First and foremost, I would like to thank my supervisor Dr. Jerry Bernholc for his continuous guidance, training and great support for my Ph.D research work. I cannot complete my research without his encouragement and advice. His enthusiasm, immense knowledge and great patience helped me continuously to accomplish my research work. The experience I learned from his guidance will be an invaluable part of my life.

I also greatly appreciate Dr. Miro Hodak and Dr. Wenchang Lu for their daily discussions about computational techniques and also great help in physics. From my Ph.D research work with them, my problem solving and analytical abilities has been enhanced greatly.

I am grateful to Dr.Zhilin Li for his helpful suggestions and valuable comments on this work. My thanks also go to my friends and coworkers, Liping Yu, Jie Jiang, Frisco Rose, Vivek Rajan, Rui Dong, Yan Li and Shuming Hu for their helpful conversations about physics and everyday help.

Finally, I want to thank my parents, my wife and my dear son for their great love and support.

TABLE OF CONTENTS

LIST OF TABLES	vi
LIST OF FIGURES	vii
Chapter 1 Methodology	1
1.1 Introduction	1
1.2 Density Functional Theory	3
1.2.1 Hohenberg-Kohn Theorem	5
1.2.2 The self-consistent Kohn-Sham Equations	8
1.2.3 Exchange-Correlation Approximation	10
1.3 Pseudopotential Approximation	12
1.3.1 Norm-Conserving Pseudopotential	14
1.3.2 Ultrasoft Pseudopotential	15
1.4 Order-N DFT Method	18
1.4.1 Matrix formulation	19
1.4.2 Computations with unoccupied orbitals	22
1.5 NEGF Method	23
1.5.1 Landauer Formula	25
1.5.2 The Green's functions and truncating the matrix	28
1.5.3 Density-functional Method for electron transport	30
1.5.4 Procedure for calculating Nonequilibrium density matrix and potential	36
1.6 Molecular Dynamics simulation	38
1.6.1 CHARMM Force Field	41
Chapter 2 Introduction	44
2.1 Introduction to DNA	44
2.2 Motivation of using DNA as an electronic material	47
2.3 DNA as a molecular wire in molecular electronics	49
2.4 DNA sensors: capable of detecting mutations and disease	50
Chapter 3 First-principles studies of conformation and solution effects on DNA transport	52
3.1 Introduction	52
3.2 Methodology	55
3.3 Results and discussion	58
3.3.1 Thermal Fluctuations in DNA Conductivity	58

3.3.2 DNA sequence effect	70
3.4 Conclusions and summary	74
References	76
Appendices	89
Appendix A Computational technique	90
A.1 Adaptive integration	90

LIST OF TABLES

Table 2.1	Geometry attribute of different forms of DNA	48
Table 3.1	Correlation coefficient of standard helicoidal DNA parameters with current for 10GC DNA.	65
Table 3.2	Correlation coefficient of standard helicoidal parameters with current for 10AT DNA	69
Table 3.3	Calculated current (nA) for different flexible sequences	71
Table 3.4	Calculated current (nA) for different sequences at site 6	72

LIST OF FIGURES

Figure 1.1	Ballistic transport scheme plot. A graphene nanoribbon field-effect transistor(GNRFET) is an example of a ballistic conductor. Contacts A and B are at different Fermi levels. Figure retrieved from http://en.wikipedia.org/wiki/File:GNRFET.png	24
Figure 1.2	We only describe a finite region of the infinite system. Inside L and R parts, the Hamiltonian matrix have the bulk electrodes values and are fixed during the self-consistent calculation. The conductor region is self-consistently updated by evaluating the charge density and Green's function calculation.	31
Figure 1.3	The closed complex contour consists of L [$\infty + i\Delta$, $EF - \gamma + i\Delta$], C , and [$EB + i\delta$, $\infty + i\delta$] enclosing the Fermi poles (black dots).	35
Figure 2.1	DNA chemical structure. The two strands of double helical DNA have opposite directions, one going from the 5' end to the 3' end, the other from the 3' end to the 5' end. The number 3' and 5' refer to the position of carbon in deoxyribose. Guanine (G) usually paired with cytosine (C) by three hydrogen bonds (shown as dotted lines); adenine (A) usually paired with thymine (T) by two hydrogen bonds. Negatively charged phosphate backbones consists of alternating phosphate groups and sugar rings. Figure retrieved from http://en.wikipedia.org/wiki/File:DNA_chemical_structure.svg	46
Figure 2.2	The structures of A (left), B (middle) and Z (right) DNA. DNA structures built from 3DNA [51].	47
Figure 3.1	The configuration of 4BP poly(G)-poly(C) DNA sandwiched between SWNT. The shaded area represents the solvent environment.	56
Figure 3.2	Histogram of calculated current for 4BP and 10BP poly(G)-poly(C) DNA	59
Figure 3.3	Histogram of calculated current of 4BP poly(G)-poly(C) DNA without explicit counterions.	60
Figure 3.4	Histogram of calculated current of 4BP poly(G)-poly(C) DNA without surrounding water molecules	61
Figure 3.5	Calculated transmission curves (left panels) and local density of states (right panels) for (a) both counterions present, (b) counterion near the phosphate group removed, (c) counterion near G4 removed. Positive counterions are shown as purple spheres. The isosurface in the right panel corresponds to the peak labeled by the blue arrow on the left panel. Dash-circled regions indicate more extended state.	62

Figure 3.6	Relation between the number of surrounding water molecules and conductivity is shown for 4BP DNA (snapshot 2). Water dipoles generally suppress the conducting state on the negatively charged phosphate groups, leading to reduced conductivity. Including more than 80 water molecules no longer changes the conductivity	63
Figure 3.7	Dependence of the conductivity of 10BP poly(G)-poly(C) DNA with the minimum overlap.	66
Figure 3.8	Isosurface of the charge density of the most conducting HOMO state from a high conductivity configuration (snapshot 15). This state is extended over most of the guanine bases.	67
Figure 3.9	Isosurface of charge density of the most conducting state from a poor conducting system (snapshot 16). The charge density is mainly localized on G1-G5.	67
Figure 3.10	The charge delocalization of the most conducting state across G5 and G6 is reduced due to smaller minimum overlap between G5 and G6.	68
Figure 3.11	Isosurface of charge distribution of a conducting state. State occupies water molecules in a 10BP poly(A)-poly(T) DNA	70
Figure 3.12	Isosurface of the charge density of the most conducting level from an optimum 10BP DNA system. The charge density of this level is uniformly delocalized through the entire system.	72
Figure 3.13	Isosurface of charge density of the most conducting state from 10BP DNA with a GT mismatched base pair at site 6. Notice the contraction of charge distribution at site 5 and 6. Counterions are not shown for simplicity.	73
Figure A.1	91

Chapter 1

Methodology

1.1 Introduction

Solutions to problems in engineering, the physical and biological sciences are using increasingly sophisticated mathematical techniques. Therefore, the bridge between mathematical sciences and other disciplines is increasingly traveled. With the great progress in new algorithms, computational methods and high performance parallel computation, it is now feasible to determine a variety of properties of a wide range of materials via fundamental equations for electrons, ions, atoms, molecules and bring insights into a lot of problems in physics, chemistry and material science.

Among the most popular computational methods, classical molecular dynamical simulation and quantum electronic structure calculations are becoming the major tools to understand the nature of materials and are useful to make predictions of real materials and understand experimentally observable phenomena. Classical molecular dynamics simulation allows us to observe important biological evolution of molecules which are difficult to observe in experiment. Quantum electronic structure is an interacting many-

body problem that must be dealt with accurately in many situations to address relevant issues. However, many ideas and fundamental approaches toward solving the problem are based on independent single particle approximations. A good combination of both classical and quantum treatment of nano-scale system provides us a great tool to understand the nature of many physical systems of interest.

The purpose of this chapter is to provide a brief exposition of the basic theory and computational methods. In this chapter, we briefly introduce Quantum Mechanics theory and the classical molecular dynamics methods that foreshadow the theoretical methods in use today.

In section 1.2, we introduce the state-of-art density functional theory, which allows one to convert a complicated interacting many-electron problem into a single particle problem by treating the electron-electron interaction with an effective potential. In section 1.3, we introduce the concept of pseudopotential by which much of the computational cost can be reduced and many problems become feasible without loss of accuracy. In section 1.4, we discuss the order-n method with optimized localized orbitals which will linearize the computational effort with the number of atoms. An overview of Non-Equilibrium Green's function (NEGF) methods and quantum transport theory is given in section 1.4. In section 1.5, we provide a brief introduction to classical molecular dynamical simulation of complicated nano-scale systems. We will also discuss the CHARMM force field which is used to describe the potential, and therefore the evolution of the system.

1.2 Density Functional Theory

Since the discovery of electrons in 1896, the theory of electrons has become one of the most challenging subjects. Electrons and nuclei are the fundamental particles that determine the nature of various materials. Electrons act like "glue" that hold repelling nuclei together and also determine various material's properties such as electrical, optical and magnetic properties.

Electrons are fermions with spin of 1/2. The principle that wave function of electrons must be antisymmetric when two electrons are exchanged was discovered by Heisenberg and Dirac [14]. Consequently, no two electrons can be in the same quantum state. This is the so-called Pauli Exclusion Principle. Fermi extended the Pauli Exclusion Principle to a formula for the statistics of non-interacting identical particles

$$f_i = \frac{1}{e^{\beta(\varepsilon_i - \mu)} \pm 1}. \quad (1.1)$$

The Hamiltonian for many-electron system is as follows:

$$H = -\frac{\hbar^2}{2m_e} \sum_j \nabla_j^2 - \frac{\hbar^2}{2M_l} \sum_l \nabla_l^2 + \frac{1}{2} \sum_{j \neq j'} \frac{e^2}{|r_j - r_{j'}|} + \frac{1}{2} \sum_{l \neq l'} \frac{Z_l Z_{l'} e^2}{|R_l - R_{l'}|} - \sum_{j,l} \frac{Z_l e^2}{|r_j - R_l|} \quad (1.2)$$

The first two terms on the right hand side of the equation are the kinetic energy operator of all the electrons and the ions. The third term is the electron-electron interaction energy. The fourth term is ion-ion interaction and the fifth term is the electron-ion interaction. We can take out the second term and fourth term which are not related to electrons. And now the Hamiltonian is much simpler

$$H = -\frac{\hbar^2}{2m_e} \sum_j \nabla_j^2 + \frac{1}{2} \sum_{j \neq j'} \frac{e^2}{|r_j - r_{j'}|} - \sum_{j,l} \frac{Z_l e^2}{|r_j - R_l|} \quad (1.3)$$

where j denotes each individual electron and l denotes each individual ion.

The reason for the simplification of the Hamiltonian is based on the Born-Oppenheimer approximation. This approximation originates from the idea that the mass of an ion is much larger than the mass of an electron and the fact that both electrons and ions are experiencing forces of the same order of magnitude. This simply means that electrons move much faster than the ions, and respond instantaneously to the movement of ions and quickly relax to the ground state for any dynamical ionic configuration. Therefore, it allows us to separate the nuclear and electronic motions.

The challenge facing physicists is to develop theoretical approaches and computational methods that can accurately describe the interacting system of many electrons and nuclei within a reasonable time scale. Enormous progress has been made in finding the approximate solutions for the many-electron Schrödinger Equation. Density Functional Theory (DFT) presented a beautiful way to accurately treat the problem in terms of electron density distribution $n(r)$. On one hand, DFT focuses on the real, 3-dimensional electron density of the ground state. And the exchange correlation hole density $n_{xc}(r, r)$ describes how the presence of an electron at r depletes the total density of the other electron at r . The understanding of this provides transparent insight into the nature of many-electron systems. On the other hand, comparing to the traditional many-body wavefunction methods where an exponential wall will be encountered when the number of atoms exceeds a critical value, DFT can solve a much bigger system of thousands of atoms. This is due to the fact that the computing time rises more moderately with the number of atoms. With an order-N method, the increase of computing time is essentially

linear with the number of atoms.

1.2.1 Hohenberg-Kohn Theorem

A. The ground state electron density $n(r)$ determines everything

The ground state density $n(r)$ of an interacting electron system in some external potential $v(r)$ uniquely determines the potential $v(r)$ up to an uninteresting additive constant. This simply means that there is a unique one to one mapping between the ground state density $n(r)$ and the external potential $v(r)$. The proof is simple and rigorous. It is presented for a non-degenerate ground state.

Let $n(r)$ be the non-degenerate ground state density of N electrons in the external potential $v_1(r)$. The corresponding ground state is Ψ_1 , and the energy is E_1 . Then, we have:

$$E_1 = (\Psi_1, H_1 \Psi_1) \tag{1.4}$$

$$= \int v_1(r)n(r)dr + (\Psi_1, (T + U)\Psi_1). \tag{1.5}$$

where H_1 is the total Hamiltonian in external potential $v_1(r)$. T is the universal kinetic operator and U is universal electron-electron interaction operator. Now let's assume that there exists another external potential $v_2(r)$, with its corresponding ground state Ψ_2 which must be different from Ψ_1 . But it gives the same ground state density $n(r)$. Then we have:

$$E_2 = (\Psi_2, H_2 \Psi_2) \quad (1.6)$$

$$= \int v_2(r) n(r) dr + (\Psi_2, (T + U) \Psi_2). \quad (1.7)$$

Given Ψ_1 is the only ground state solution of H_1 , we have

$$E_1 < (\Psi_2, H_1 \Psi_2) \quad (1.8)$$

$$= \int v_1(r) n(r) dr + (\Psi_2, (T + U) \Psi_2) \quad (1.9)$$

$$= E_2 + \int [v_1(r) - v_2(r)] n(r) dr. \quad (1.10)$$

Similarly,

$$E_2 \leq (\Psi_1, H_2 \Psi_1) \quad (1.11)$$

$$= \int v_2(r) n(r) dr + (\Psi_1, (T + U) \Psi_1) \quad (1.12)$$

$$= E_1 + \int [v_2(r) - v_1(r)] n(r) dr. \quad (1.13)$$

The reason we use \leq is that the non-degeneracy is not assumed for Ψ_2 with the total Hamiltonian being H_2 . Combining the above two equations, we come to an obvious contradiction

$$E_1 + E_2 < E_1 + E_2 \quad (1.14)$$

Therefore, the assumption that there exist two external potentials that share the same ground state density $n(r)$ must be wrong. Provided that $n(r)$ determines both N and $v(r)$, it also determines the total H and implicitly all the properties derivable from H .

B. The Hohenberg-Kohn variational principle

The most significant property of a particular electronic ground state is its total energy E which can be obtained by either solving the Schrödinger equation $H\Psi = E\Psi$ or from minimizing

$$E = \min_{\tilde{\Psi}}(\tilde{\Psi}, H\tilde{\Psi}) \quad (1.15)$$

where $\tilde{\Psi}$ is the normalized trial function for N electrons to minimize the total energy. The trial density $\tilde{n}(r)$ can be obtained by integrating the $\tilde{\Psi}^* \tilde{\Psi}$ over all variables except the first and multiplying by N . Therefore, we can decompose the minimization process into two steps. First, let's fix the $\tilde{n}(r)$ and denote by $\tilde{\Psi}_n^\alpha$ the trial function that integrates to $\tilde{n}(r)$. We define the constrained minimized total energy as

$$E_v[\tilde{n}(r)] = \min_{\alpha}(\tilde{\Psi}_n^\alpha, H\tilde{\Psi}_n^\alpha) \quad (1.16)$$

$$= \int v(r)\tilde{n}(r)dr + F[\tilde{n}(r)] \quad (1.17)$$

where

$$F[\tilde{n}(r)] = \min_{\alpha}[\tilde{\Psi}_n^\alpha, (T + U)\tilde{\Psi}_n^\alpha] \quad (1.18)$$

$F[\tilde{n}(r)]$ is not related to $v(r)$, therefore it is a universal function of $\tilde{n}(r)$. So the next step is to minimize the total energy over all possible $\tilde{n}(r)$

$$E = \min_{\tilde{n}(r)} E_v[\tilde{n}(r)] \quad (1.19)$$

$$= \min_{\tilde{n}(r)} \left\{ \int v(r)\tilde{n}(r)dr + F[\tilde{n}(r)] \right\} \quad (1.20)$$

Now, the formidable problem of minimizing the total energy of a $3N$ dimensional many-body system is greatly simplified into finding the 3 dimensional density function $n(r)$ which minimizes the total energy. $F[\tilde{n}(r)]$ is a well defined but not explicitly known functional of density. It represents the sum of kinetic energy and interaction energy.

An approximation could be made by rederiving the Thomas-Fermi (TF) theory

$$T = \int n(r) \frac{3}{10} k_F^2[n(r)] dr \quad (1.21)$$

$$U = \frac{1}{2} \int \frac{n(r)n(r')}{|r-r'|} dr dr' \quad (1.22)$$

where $K_F(n)$ is the Fermi wave vector of a uniform electron gas with density n and $\frac{3}{10}k_F^2[n]$ is the corresponding mean kinetic energy per electron. U represents the classic mean-field coulomb's interaction energy. The error is mainly due to poor description of the kinetic energy T .

1.2.2 The self-consistent Kohn-Sham Equations

Kohn and Sham decomposed $K_F(n)$ into three parts

$$F[\tilde{n}(r)] = T_s[\tilde{n}(r)] + \frac{1}{2} \int \frac{\tilde{n}(r)\tilde{n}(r')}{|r-r'|} dr dr' + E_{xc}[\tilde{n}(r)] \quad (1.23)$$

where $T_s[\tilde{n}(r)]$ is the kinetic energy functional. The second term is the coulomb interaction energy and the last term is the so-called exchange-correlation energy. The Hohenberg-Kohn variational principle with the corresponding Euler-Lagrange multipliers ε make sure the total number of electrons are conserved under the variation

$$\delta E_v[\tilde{n}(r)] = \int \delta \tilde{n}(r) \left\{ v_{eff}(r) + \frac{\delta}{\delta \tilde{n}(r)} T_s[\tilde{n}(r)] \Big|_{\tilde{n}(r)=n(r)} - \varepsilon \right\} dr = 0 \quad (1.24)$$

where

$$v_{eff}(r) \equiv v(r) + \int \frac{n(r')}{|r-r'|} dr' + v_{xc}(r) \quad (1.25)$$

and

$$v_{xc}(r) \equiv \frac{\delta}{\delta \tilde{n}(r)} E_{xc}[\tilde{n}(r)] \Big|_{\tilde{n}(r)=n(r)} \quad (1.26)$$

From 1.24 and the fact that

$$\frac{\delta \tilde{n}(r)}{\delta \psi_j^*(r)} \Big|_{\tilde{n}(r)=n(r)} = \psi_j(r) \quad (1.27)$$

we can naturally conclude that $n(r)$ can be obtained by solving the single-particle equation

$$\left(-\frac{1}{2} \nabla^2 + v_{eff}(r) - \varepsilon_j \right) \psi_j(r) = 0 \quad (1.28)$$

with

$$n(r) = \sum_{j=1}^N |\psi_j(r)|^2 \quad (1.29)$$

$$v_{eff}(r) = v(r) + \int \frac{n(r')}{|r - r'|} dr' + v_{xc}(r) \quad (1.30)$$

where $v_{xc}(r)$ is the exchange-correlation potential depending on the function $n(r)$. The ground state total energy of any system is given by

$$E = \sum_{j=1}^N \varepsilon_j + E_{xc}[n(r)] - \int v_{xc}(r)n(r)dr - \frac{1}{2} \int \frac{n(r)n(r')}{|r - r'|} drdr' \quad (1.31)$$

The equations 1.28 - 1.31 are called Kohn-Sham (KS) equations. In the Kohn-Sham ansatz, the electrons move independently from each other except that they feel the effective field from the other electrons and ions.

1.2.3 Exchange-Correlation Approximation

How to treat the electron-electron interaction accurately through the exchange correlation energy, turns out to be the most challenging problem of the field of Electronic Structure today. Many approaches have been used to improve the exchange-correlation energy functional. Here, we briefly introduce the local density approximation (LDA) and the generalized gradient approximation (GGA)[69] [68].

Local Density Approximation

The LDA approximation is the simplest approximation among all. It is based on the idea that the exchange-correlation energy $\varepsilon_{xc}(r)$ per electron at a point r is approximated by the exchange-correlation energy $\varepsilon_{xc}^{hom}[n(r)]$ of a homogeneous electron gas with uniform

density. LDA assumes that the exchange-correlation energy functional is essentially local

$$E_{xc}^{LDA}[n(r)] = \int n(r)\varepsilon_{xc}^{hom}[n(r)]dr. \quad (1.32)$$

LDA ignores the corrections to the exchange-correlation energy due to the variation in $n(r)$, so it was expected to be useful only for system in which the density varies slowly on the scale of the local Fermi wavelength. However, it has been surprisingly successful for total energy calculation in most applications. This is due to the fact the LDA satisfies the sum rule which express the normalization of the exchange-correlation hole.

Generalized Gradient Approximation

Although the LDA works very well in many solid state systems, it fails in systems which lack any resemblance to noninteracting electron gas, such as the electronic Wigner crystal and molecules with tight bonding. Generalized gradient approximation (GGA) was introduced targeting the incorporation of the effects of inhomogeneities by including the gradient component of the density

$$E_{xc}^{GGA}[n(r)] = \int n(r)\varepsilon_{xc}^{hom}[n(r)]F_{xc}[n(r), \nabla n(r)]dr. \quad (1.33)$$

$F_{xc}[n(r), \nabla n(r)]$ is the enhancement factor. There are many efforts towards getting the best form for the enhancement factor. Perdew, Burke and Ernzerhof(PBE) [69] have devised a PBE functional which uses a very simplified exchange enhancement factor in the form

$$F_x^{PBE}(s) = 1 + \kappa - \frac{\kappa}{1 + \mu s^2 / \kappa} \quad (1.34)$$

where $s(r)$ is the dimensionless reduced charge density gradient

$$s(r) = \frac{|\nabla n(r)|}{2K_F(r)n(r)} \quad (1.35)$$

with

$$K_F(r) = [3\pi^2 n(r)]^{1/3} \quad (1.36)$$

GGA construction has made use of sum rules, general scaling properties, asymptotic behavior of the effective potential, and densities in the tail region of atoms and their aggregates.

1.3 Pseudopotential Approximation

One of the difficulties of DFT is to treat accurately both the electrons close to nuclei and electrons in the smooth bonding regions. Since only electrons close to Fermi level will participate in electrical conduction, heat capacity and other phenomena, the pseudopotential method, which deals only with valence electrons, solves this problem. The use of pseudopotentials helps us to reduce the computational cost by dealing with only outer shell electrons, and providing a smoother external potential. If we were to represent the highly localized wavefunctions of those core electrons, the computational load would be formidable due to the increase of number of electrons to deal with and due to the very strong core electron interaction with the nuclear potential.

Orthogonalized plane wave (OPW) formalism, introduced by Herring[33, 34] in 1940,

is very helpful in understanding the concept of pseudopotential. The theorem sets the requirement that the valence states should be orthogonal to the core states. This orthogonalization provides an effective repulsive potential for the valence states. Therefore, the repulsive potential almost cancels out the attractive potential exerted by the positive core region, leaving a relatively smooth potential for the valence electrons.

In the OPW methods, the valence states are expressed as the sum of a smooth function ϕ and a sum of all core states ϕ_c

$$|\Psi\rangle = |\phi\rangle + \sum_c \alpha_c |\phi_c\rangle \quad (1.37)$$

Since the valence states Ψ is orthogonal to the core states ϕ_c , we have

$$|\Psi\rangle = |\phi\rangle - \sum_c |\phi_c\rangle \langle \phi_c | \phi \rangle \quad (1.38)$$

Assume that Ψ satisfies the Schrödinger equation:

$$H |\Psi\rangle = (T + V_c) |\Psi\rangle = E |\Psi\rangle \quad (1.39)$$

where T is the kinetic energy operator and V_c represents the attractive core potential. Combining the above two equations, we have

$$H |\phi\rangle + \sum_c (E - E_c) |\phi_c\rangle \langle \phi_c | \phi \rangle = E |\phi\rangle \quad (1.40)$$

given that, E_c is the eigen energy of the core state ϕ_c

$$H |\phi_c\rangle = E_c |\phi_c\rangle \quad (1.41)$$

Then the Schrödinger equation can be rewritten as

$$T + V^{ps} |\phi\rangle = E |\phi\rangle \quad (1.42)$$

where

$$V^{ps} = V_c + \sum_c (E - E_c) |\phi_c\rangle \langle \phi_c| \quad (1.43)$$

[71]

1.3.1 Norm-Conserving Pseudopotential

The purpose is to get a pseudized smooth solution ϕ instead of the highly varied true solution Ψ . The so-called norm-conserving pseudopotential is constructed in such a way that it matches the true potential outside the core radius. The pseudo-wavefunctions also must match the true wavefunction outside the core radius. The eigenvalues calculated using the pseudopotential should be equal to the true eigenvalues obtained from the all-electron calculations. Moreover, the charge density match the true charge density outside this region. Lastly, the integration of charge density over the core region should be the same.

The true wavefunctions are constructed from all-electron DFT calculations as a reference. The resulting pseudized valence wavefunctions are obtained by removing the oscillations in the core region while obeying the norm-conserving constraint. The Schrödinger equation is then inverted to look for pseudopotential which will reproduce the pseudized valence wavefunctions[29].

1.3.2 Ultrasoft Pseudopotential

There has been a rapid growth of first-principle calculations with the advent of norm-conserving pseudopotentials [29, 45] in the last three decades. The constraint of norm-conserving pseudopotentials is that the charge inside of a cutoff radius r_c should be equal to the charge obtained from all-electron calculations. However, this constraint, in certain cases such as *O*'s $2p$ or *Ni*'s $3d$ orbitals [83], becomes an obstacle to construct a smooth pseudo wavefunction. Vanderbilt introduced a new scheme to generate the so-called ultrasoft pseudopotentials (UPPs) in early 1990s.

In his UPP method, the norm-conserving constraint is relaxed, and the pseudo wave functions are allowed to be as soft as possible within the core region. Therefore, the energy cutoff required to represent the wave functions is reduced dramatically. The implementation of UPP enables efficient calculations of the atomic electronic structures and electron transport properties of nano-scale systems.

The Vanderbilt UPP has the norm-conserving constraint relaxed:

$$\int_0^{r_c} \psi_n^*(r)\psi_m(r) - \int_0^{r_c} \phi_n^*(r)\phi_m(r) \neq 0 \quad (1.44)$$

where $\psi_n(r)$ are the all-electron wavefunctions and $\phi_n(r)$ are the pseudo wavefunctions. This relaxation provides capability in the construction of smooth pseudo waves inside the core region. Therefore, the new augmentation functions, namely, $Q_{n,m}^I(r)$ are defined as:

$$Q_{n,m}^I(r) = Q_{n,m}(r - R_I) = \psi_n^*(r)\psi_m(r) - \phi_n^*(r)\phi_m(r) \quad (1.45)$$

which describe the charge density difference between true and pseudo valence orbitals. We should notice that the augmentation functions are strictly zero outside the core region, so

$Q_{n,m}^I(r)$ are localized in the core region only. In order to recover the electronic charge, the electron charge density of the squared moduli of the pseudo wavefunctions is augmented in the core region by the following:

$$n(r) = \sum_i \left[|\phi_i(r)|^2 + \sum_{nm} Q_{n,m}^I(r) \langle \phi_i(r) | \beta_n^I \rangle \langle \beta_m^I | \phi_i(r) \rangle \right] \quad (1.46)$$

Here $\beta_n^I = \beta_n(r - R_I)$ are projector functions centered on the ionic positions and vanish outside the core region. For UPP, two projectors are often required for each angular momentum channel. Therefore, the total number of projectors is generally twice as many as that for a norm-conserving pseudopotential.

In addition, the orthonormality condition for the wavefunctions takes on a generalized form due to the relaxation of the norm-conserving condition,

$$\langle \phi_i | S(R_I) | \phi_j \rangle = \delta_{ij} \quad (1.47)$$

where the Hermitian overlap operator S depends on the ionic positions via the projector functions $|\beta_n^I\rangle$ and is defined by

$$S(R_I) = 1 + \sum_{nm,I} q_{nm} |\beta_n^I\rangle \langle \beta_m^I| \quad (1.48)$$

with

$$q_{nm} = \int Q_{nm}(r) dr \quad (1.49)$$

The total energy functional in Vanderbilts UPP scheme is given by

$$E_{tot}[\phi_i, R_I] = \sum_{i=1}^N \langle \phi_i | -\frac{1}{2}\nabla^2 + V_{NL} | \phi_i \rangle + \frac{1}{2} \int \frac{n(r)n(r')}{|r-r'|} dr dr' \quad (1.50)$$

$$+ \int dr V_{loc}^{ion}(r)n(r) + E_{xc}[n(r)] + E_{ion}(R_I)$$

with

$$V_{NL} = \sum_{nm,I} D_{nm}^{(0)} |\beta_n^I\rangle \langle \beta_m^I| \quad (1.51)$$

where $D_{nm}^{(0)}$ are also parameters characterizing the UPP. The minimization of this total energy functional which is subject to the new constraint leads to a generalized eigenvalue problem

$$H |\phi_i\rangle = \varepsilon_i S |\phi_i\rangle \quad (1.52)$$

where

$$H = -\frac{1}{2}\nabla^2 + V_{eff} + \sum_{nm,I} D_{nm}^I |\beta_n^I\rangle \langle \beta_m^I| \quad (1.53)$$

with the $V_{eff}(r)$ completely local

$$V_{eff}(r) = V_{loc}^{ion}(r) + V_H + V_{XC} \quad (1.54)$$

and the coefficient D_{nm}^I of the nonlocal part of UPP is given by

$$D_{nm}^I = D_{nm}^{(0)} + \int V_{eff}(r) Q_{nm}^I(r) dr \quad (1.55)$$

Apparently, the UPPs have a fully separable form of the non-local pseudopotential, and the coefficients depending on the wavefunctions via V_{eff} have to be updated at each self-consistent step.

The ultrasoft pseudopotential will be thus fully determined once the quantities V_{loc} , D_{nm} , $Q_{nm}(r)$ and $\beta_n(r)$ are specified. The detailed procedure used to generate these quantities is described in [83]. Comparing with the norm-conserving pseudopotential, the relaxation of the norm-conserving condition results in the introduction of the S overlap operator, the generalization of the eigenvalue equation, the wavefunction dependence of the coefficients D_{nm}^I , and the increase of the number of projector functions, but it makes the wavefunctions much smoother inside the core region and therefore allows for lower cutoff energies to represent the wavefunctions. In most cases, the cutoff energy is about half that of conventional norm-conserving pseudopotentials when ultrasoft pseudopotentials are used. Such advantage puts the UPPs on the top list of the most widely used pseudopotentials in the field of modern condensed matter ab-initio calculations.

1.4 Order-N DFT Method

The expansions of the wave functions can be generally divided into two classes. In the basis of plane waves, its kinetic energy is diagonal in Hamiltonian. In the basis of real space, the local potential is diagonal. The real-space grid method can lead to easier parallelization using domain decomposition on massively parallel supercomputers. Moreover, real-space is necessary for the implementation of $O(N)$ techniques, which reduce computational cost from $O(N^3)$ to much lower linear cost with respect to the number of atoms. These techniques are based on optimized nonorthogonal orbitals which are very much localized in space. Therefore, the overlaps between functions far away from each other vanish. The total number of overlaps is $O(N)$. Fully self-consistent $O(N)$ DFT calculations with atomic-like orbitals as basis have been previously developed in our group [16, 60, 50]. With our real-space oriented approach, the unoccupied states can

be included to accelerates the convergence. Several similar works has already been done [32, 31, 37]. A multigrid preconditioner is also included for efficient iterative minimization. We also use a compact and accurate Mehrstellen finite difference (MFD) scheme, which has already been introduced in electronic calculations. [9] Finally, the optimized localized orbitals enable the efficient calculations of quantum transport properties, which rely on the expansion of Hamiltonian and Green's function matrices in terms of localized orbitals.

1.4.1 Matrix formulation

This subsection describes the general matrix formulation for the iterative DFT calculation using grid-based localized orbitals. Let N denote the number of wave functions we need to solve for and M denote the number of grid points used to discretized the total system. Usually we have $M \gg N$.

We need to solve

$$H\psi_j = [-\frac{1}{2}\nabla^2 + v_{ion} + v_H + v_{xc}]\psi_j \quad (1.56)$$

where $\Psi = (\psi_1, \dots, \psi_N)$ are the set of orthonormal eigen-functions of the K-S equation. Assume that we have a set of normalized but nonorthogonal trial functions $\Phi = (\phi_1, \dots, \phi_N)$ that will span the subspace of the occupied orbitals. We denote by C the $N \times N$ transformation matrix that transform Φ into Ψ

$$\Psi = (\psi_1, \dots, \psi_N) = \Phi C \quad (1.57)$$

Therefore, given that Ψ are orthonormal, we have

$$I = \Psi^T \Psi = C^T \Phi^T \Phi C = C^T S C \quad (1.58)$$

where

$$S = \Phi^T \Phi \quad (1.59)$$

so

$$CC^T = S^{-1} \quad (1.60)$$

Moreover, since Ψ are orthonormal eigen-solutions of H , we have

$$\Lambda = \Psi^T H \Psi \quad (1.61)$$

where Λ is a $N \times N$ diagonal matrix, with eigenvalues on the diagonal. From equation 1.61 and equation 1.57, we can easily get

$$\Lambda = C^T \Phi^T H \Phi C \quad (1.62)$$

$$= C^T H^{(\Phi)} C \quad (1.63)$$

Therefore, it leads us to the generalized eigenvalue problem

$$H^{(\Phi)} C = C^{-T} \Lambda \quad (1.64)$$

$$= SC \Lambda \quad (1.65)$$

In the basis of Ψ , the energy functional decreases at the fastest rate along SD directions. They are the negative residual of the Kohn-Sham equation and can be expressed in a $M \times N$ matrix

$$D^{(\Psi)} = \Psi \Lambda - H \Psi, \quad (1.66)$$

At each iteration, Λ is determined by the condition that the following equation

$$0 = \Psi^T D^{(\Psi)} = \Psi^T \Psi \Lambda - \Psi^T H \Psi \quad (1.67)$$

has to be satisfied for good convergence. Once we know the direction $D^{(\Psi)}$, then the next Ψ^{new} can be computed with pseudo time step η and a linear preconditioning operator K

$$\Psi^{new} = \Psi + \eta K D^{(\Psi)} \quad (1.68)$$

Without preconditioning, the stability of the iterative process depends on η being small.

Now, let's preserve the SD direction and work with nonorthogonal basis Φ . The simplest way to obtain the SD direction in the Φ basis is to use the matrix C

$$D^{(\Phi)} = D^{(\Psi)} C^{-1} \quad (1.69)$$

$$= (\Psi \Lambda - H \Psi) C^{-1} \quad (1.70)$$

$$= \Phi \Theta - H \Phi \quad (1.71)$$

where

$$\Theta = S^{-1} H^{(\Phi)} \quad (1.72)$$

The preconditioned steepest descend (PSD) direction tells us how to update the next Φ

$$\Phi^{new} - \Phi = \eta K D^{(\Phi)} = \eta K (\Phi \Theta - H \Phi) \quad (1.73)$$

Note that in the whole iterative process, there is no need to solve the generalized eigenvalue problems. At each step the basis functions Φ are updated according to 1.73, and

the electronic density is computed as

$$\rho(r) = 2 \sum_{j,k=1}^N (s^{-1})_{jk} \phi_j(r) \phi_k(r) \quad (1.74)$$

To get the first term on the right hand side of equation 1.31, we can do

$$\sum_{j=1}^N 2\varepsilon_j = 2Tr(\Lambda) = 2Tr(\Theta) \quad (1.75)$$

due to similarity-invariant

$$Tr(\Theta) = Tr(C\Lambda C^{-1}) = Tr(C^{-1}C\Lambda) = Tr(\Lambda) \quad (1.76)$$

1.4.2 Computations with unoccupied orbitals

Inclusion of unoccupied orbitals substantially increases the convergence rate. Now we denote N as the sum of both occupied and unoccupied orbitals counts. But in order to calculate the electron density and total energy, a density-matrix formalism need to be introduced here. μ denotes the chemical potential. $N \times N$ diagonal matrix Υ incorporates the Fermi-Dirac distribution.

$$\Upsilon_{ij} = \delta_{ij} f[(\varepsilon_i - \mu)/k_B T] \quad (1.77)$$

Then, the density operator $M \times M$ matrix $\hat{\rho}$ is given by

$$\hat{\rho} = \Psi \Upsilon \Psi^T \quad (1.78)$$

It will be natural to express the density operator on the Φ basis since it will dramatically shrink its size to $N \times N$ matrix

$$\rho^{(\Phi)} = \Phi^T \hat{\rho} \Phi = \Phi^T \Psi \Upsilon \Psi^T \Phi \quad (1.79)$$

$$= \Phi^T \Phi C \Upsilon C^T \Phi^T \Phi \quad (1.80)$$

$$= S C \Upsilon C^T S \quad (1.81)$$

$$= C^{-T} \Upsilon C^{-1} \quad (1.82)$$

As in [62], we introduce $\bar{\rho}^{(\Phi)}$

$$\bar{\rho}^{(\Phi)} = S^{-1} \rho^{(\Phi)} S^{-1} = C \Upsilon C^T \quad (1.83)$$

This facilitates the calculation of expectation value of any physical properties using

$$\bar{A} = 2Tr(\Upsilon A^{(\Psi)}) = 2Tr(\bar{\rho}^{(\Phi)} A^{(\Phi)}) \quad (1.84)$$

For instance, the number of occupied electrons in the system is given by

$$N_e = 2Tr(\Upsilon I) = 2Tr(C \Upsilon C^{-1}) = 2Tr(C \Upsilon C^T S) = 2Tr(\bar{\rho}^{(\Phi)} S) \quad (1.85)$$

1.5 NEGF Method

The purpose of this chapter is to describe a method to calculate the electron transport in nano-scale system. Consider a conductor sandwiched between two large contacts. If the dimension of the conductor is large, the conductance would be given by $G = \sigma W/L$ where W is the width and L is the length and σ depends on the material. Thus, we would

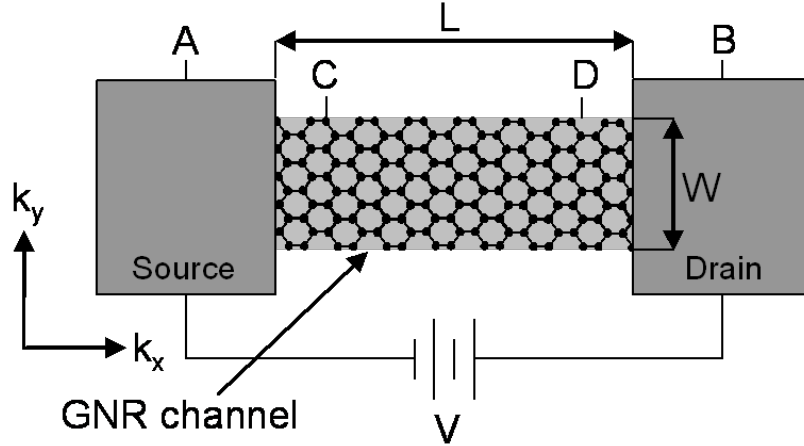


Figure 1.1: Ballistic transport scheme plot. A graphene nanoribbon field-effect transistor(GNRFET) is an example of a ballistic conductor. Contacts A and B are at different Fermi levels. Figure retrieved from <http://en.wikipedia.org/wiki/File:GNRFET.png>

expect that the conductance will grow indefinitely as we shrink its length. Experimentally, however, the conductance will approach to a limiting value G_c when the length becomes much shorter than the mean free path but still much longer than the phase-relaxation length. After all, a ballistic conductor without any scattering should in principle have no resistance. This resistance comes from the interface between the contact pads and the conductor where it requires the redistribution of the current among the current-carrying modes.

Let us consider to calculate the current through a ballistic conductor with different chemical potential μ_A in the left contact, and μ_B in the right contact as shown in Figure 1.1. Lets assume that the contacts are reflectionless: $+k$ states in the conductor are occupied by electrons coming from the left contact while $-k$ states are occupied by electrons coming from the right contact. Lets try to simplify the problem further by considering a single transverse mode conductor whose $+k$ states occupied according to

$f^+(E)$ with chemical potential μ_A . The current which is equal to env can be written as:

$$I = \frac{e}{L} \sum_k v f(E) = \frac{e}{L} \sum_k \frac{1}{\hbar} \frac{\delta E}{\delta k} f(E) = \frac{e}{\hbar L} 2(\text{for spin}) \frac{L}{2\pi} \int dk \frac{\delta E}{\delta k} f(E) = \frac{2e}{h} \int_{\epsilon}^{\infty} f(E) dE \quad (1.86)$$

since the electron density associated with the single k state in the conductor of length L is just $\frac{1}{L}$.

1.5.1 Landauer Formula

The conductance of large conductor obeys an ohmic law: $G = \sigma W/L$, but as the dimension goes smaller and smaller, there are two corrections to this law. First there is an interface resistance and secondly the conductance depends on the number of transverse modes in the conductor which goes down discretely in steps as the width shrinks.

$$G = \frac{2e^2}{h} MT \quad (1.87)$$

Where T represents the transmission probability that an electron injected from one end of the conductor will transmit to the other end, and M represents the number of such modes. M usually plays a significant role in narrow conductor. As the width of the conductor was reduced, the conductance goes down in discrete steps.

For simplicity, let's assume zero temperature. So the current flow takes place over the range between μ_A and μ_B . The influx of electrons from contact A is

$$I_A^+ = \frac{2e}{h} M [\mu_A - \mu_B] \quad (1.88)$$

The outflux from contact B is just the influx from contact A times the transmission probability T :

$$I_B^+ = \frac{2e}{h}MT[\mu_A - \mu_B] \quad (1.89)$$

while the rest of the flux is reflected back to contact A:

$$I_A^- = \frac{2e}{h}M(1 - T)[\mu_A - \mu_B] \quad (1.90)$$

Therefore the net current I flowing in the device at any point is given by

$$I = I_A^+ - I_A^- = I_B^+ = \frac{2e}{h}MT[\mu_A - \mu_B] \quad (1.91)$$

Hence the conductance is

$$G = \frac{I}{[\mu_A - \mu_B]/|e|} = \frac{2e^2}{h}MT \quad (1.92)$$

We can extend the system from zero temperature to non-zero temperature. Now the current flow takes place at a slightly larger range

$$\mu_A + (\text{a few } K_B T) > E > \mu_B - (\text{a few } K_B T) \quad (1.93)$$

and the net current $i(E)$ flowing at any point is given by

$$i(E) = i_A^+ - i_A^- = \frac{2e}{h}[\bar{T}(E)f_A(E) - \bar{T}'(E)f_B(E)] \quad (1.94)$$

where $\bar{T}(E) = M(E)T(E)$ and if we assume there is no inelastic scattering, we will have

$\bar{T}(E) = \bar{T}'(E)$ for a two terminal device. The formula can be rewritten as

$$i(E) = \frac{2e}{h} \bar{T}(E) [f_A(E) - f_B(E)] \quad (1.95)$$

and

$$I = \int i(E) dE \quad (1.96)$$

If both contacts are held at the same potential which means $\mu_A = \mu_B$ then we have zero current since $f_A(E) = f_B(E)$. Now let's assume μ_A is just a little larger than μ_B . The current will be

$$\delta I = \frac{2e}{h} \int \bar{T}(E) \delta[f_A - f_B] dE = \frac{2e}{h} \int \bar{T}(E) \left(-\frac{\delta f}{\delta E}\right) [\mu_A - \mu_B] dE \quad (1.97)$$

At low temperature, we have $-\frac{\delta f}{\delta E} = \delta(E_f - E)$. Therefore the conductance reduces to linear response form:

$$G = \frac{2e^2}{h} \bar{T}(E_f) \quad (1.98)$$

The linear response result is only valid when the bias is smaller than the sum of $K_B T$ and correlation energy ε_c :

$$\mu_A - \mu_B \ll K_B T + \varepsilon_c \quad (1.99)$$

The Landauer-Buttiker formalism is valid for coherent transport where the exclusion principle should not be considered. When there is elastic scattering taking place, we can also regard the scatterer as a virtual probe in the system, and calculate the current at the same footing as the contacts, although its net current is zero. Elastic scattering does not involve any vertical flow of current from one energy to another. The transmission functions can be calculated using phenomenological approaches.

$$\bar{T}_{AB}^{eff} = \bar{T}_{AB} + \bar{T}_{A\psi}\bar{T}_{\psi B} \quad (1.100)$$

where ψ represent the elastic scatterer. So the overall effective transmission can be sum up by both the direct coherent transport where electrons go coherently from contact A to contact B and the indirect transport where electrons go from contact A to the scatterer coherently, suffering a phase-breaking process, then continue to contact B coherently. The Landauer-Buttiker formalism still holds in this case except with a different effective transmission coefficient. Even if the vertical flow is present, it can be neglected if the transmission functions are approximately constant over the energy range where transport occurs.

1.5.2 The Green's functions and truncating the matrix

The Green's function is a more powerful tool. It relates to the response at any point due to an excitation from another point. Assume that we have an excitation S , and the response is Ψ . The problem can be expressed as

$$[E - H]\Psi = S \quad (1.101)$$

The corresponding Green's functions is

$$G = [E - H]^{-1} \quad (1.102)$$

If the system is open, G will not be representable. How to truncate the open system, namely the semi-infinity leads, into a finite closed system is very important. We need to convert the open system with non-reflecting boundaries to a closed system with fully

reflecting boundaries. Consider a conductor connected to a lead p as shown below.

We can divide the system's Green's function into four sub-matrices as follows:

$$\begin{bmatrix} G_p & G_{pC} \\ G_{Cp} & G_C \end{bmatrix} = \begin{bmatrix} EI - H_p & \tau_p \\ \tau_p^+ & EI - H_C \end{bmatrix}^{-1} \quad (1.103)$$

where $EI - H_p$ represents the isolated lead, $EI - H_C$ represents the isolated conductor and τ_p represents the coupling between points from the conductor and points from the lead. We assume the coupling only exists for adjacent points across the interface.

$$\tau_p(p_i, i) = t \quad (1.104)$$

We are only interested in the closed Green's function G_C , which describes the relation between any two points in the conductor with the effect of the infinite lead included. From (1.103), we have

$$[EI - H_p]G_{pC} + [\tau_p]G_C = 0 \quad (1.105)$$

and

$$[EI - H_c]G_C + [\tau_p^*]G_{pC} = I \quad (1.106)$$

If we cancel G_{pC} , we obtain

$$G_C = [EI - H_C - \tau_p^* g_p^R \tau_p]^{-1} \quad (1.107)$$

where

$$g_p^R = [EI - H_p]^{-1} \quad (1.108)$$

is the Green's function for the isolated semi-infinite lead. Now G_C is a finite matrix with

size $C \times C$, C being the number of grid points in conductor. The lead effect is taken into account through term $\tau_p^* g_p^R \tau_p$, the so-called self-energy term. If we have multiple leads, the term is additive. So

$$G_C = [EI - H_C - \Sigma^R]^{-1} \quad (1.109)$$

where the self-energy is

$$\Sigma^R = \sum_p \Sigma_p^R = \sum_p t^2 g_p^R \quad (1.110)$$

1.5.3 Density-functional Method for electron transport

In this section, we describe the ab initio method for calculating the electronic structure and electronic transport for atomic system connected to semi-infinite leads. This method is based on DFT. The valence states are based on finite-range atomic orbitals. We use not only the total charge density, but also the Kohn-Sham wave functions as single-particle wave functions when calculating the current. We assume the XC functionals are able to describe the electrons in the nonequilibrium situations where current flow exists. Here, inelastic scattering, for instance, by phonons [61], is not considered. The great advantage of using finite-range nonorthogonal orbitals as the basis is that the Hamiltonian interactions go to zero beyond some distance, which allows us to partition the overall system.

We will consider the case as in Figure 1.2. Two semi-infinite leads are connected with a contact from both sides. The left lead is far away from the right lead so that there is no direct interaction between them. We can test this assumption by including part of the leads in contact region. We need a finite Green's function to describe the open system

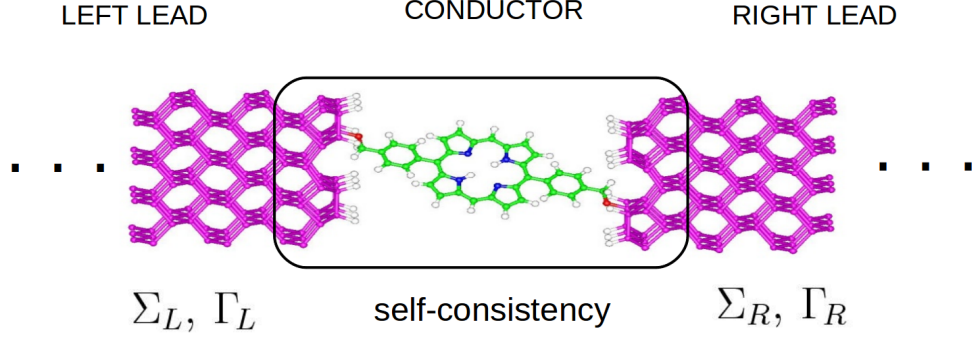


Figure 1.2: We only describe a finite region of the infinite system. Inside L and R parts, the Hamiltonian matrix have the bulk electrodes values and are fixed during the self-consistent calculation. The conductor region is self-consistently updated by evaluating the charge density and Green's function calculation.

by inverting the finite matrix,

$$\begin{bmatrix} H_L + \Sigma_L & V_L & 0 \\ V_L^\dagger & H_C & V_R \\ 0 & V_R^\dagger & H_R + \Sigma_R \end{bmatrix} \quad (1.111)$$

Here, H_L , H_R and H_C are the Hamiltonian matrices in the L (left lead), R(right lead) and C (the conductor region). V_L (V_R) is the interaction between the L (R) and C. Σ_L and Σ_R are the self energies of the leads.

$H_L + \Sigma_L$ and $H_R + \Sigma_R$ are determined from two separate calculations for the bulk systems corresponding to the bulk of infinite left lead and right lead. These systems have periodic boundary conditions in x direction and are solved using Bloch's theorem. The self energies of the leads are determined by cutting the infinite lead system into two semi-infinite pieces using either the ideal construction[88] or the efficient recursion method[79].

The remaining part of the Hamiltonian, namely, V_L , V_R and H_C are determined by self-consistently calculating nonequilibrium electron charge density. We will show how the nonequilibrium electron charge density matrix can be calculated given these parts of Hamiltonian and how the Hamiltonian matrix elements are calculated from the density matrix. Let's consider the scattering states ψ_l^0 starting in the left lead. They are generated from the unperturbed incoming states of the uncoupled, semi-infinite lead. Using the retarded Green's function G of the coupled system, we will have

$$\psi_l(\vec{x}) = \psi_l^0(\vec{x}) + \int d\vec{y} G(\vec{x}, \vec{y}) \psi_l^0(\vec{y}) \quad (1.112)$$

and due to the fact that there is no direct interaction between the two leads we will have

$$V_R(\vec{r})\psi_l(\vec{r}) = V_L(\vec{r})\psi_r(\vec{r}) = 0 \quad (1.113)$$

Our nonequilibrium situation is established by the following scenario: All the states deep in the left/right leads are filled up to the electrochemical potential of the left/right lead, namely, μ_L and μ_R . Therefore the density matrix of the incoming scattering states from the left and right lead can be constructed as

$$D(\vec{x}, \vec{y}) = \sum_l \psi_l(\vec{x}) \psi_l^*(\vec{y}) n_F(\varepsilon_l - \mu_L) + \sum_r \psi_r(\vec{x}) \psi_r^*(\vec{y}) n_F(\varepsilon_r - \mu_R) \quad (1.114)$$

Here the density matrix only describes states in C which couple to the leads.

Now we will represent density matrix in terms of nonorthogonal localized orbitals.

$$\psi_l(\vec{x}) = \sum_{\mu} c_{l\mu} \phi_{\mu}(\vec{x}) \quad (1.115)$$

So the above density matrix can be rewritten in orbital representation as:

$$D_{\mu,v} = \sum_l c_{l\mu} c_{lv}^* n_F(\varepsilon_l - \mu_L) + \sum_r c_{r\mu} c_{rv}^* n_F(\varepsilon_r - \mu_R) \quad (1.116)$$

where

$$c_{l\mu} = c_{l\mu}^0 + \sum_v [G(z)V]_{\mu v} c_{lv}^0 \quad (1.117)$$

The overlap between orbitals is handled by defining the Green's function as the inverse of $zS - H$. So

$$[zS - H]G(z) = 1 \quad (1.118)$$

It is convenient to introduce the spectral density matrix ρ_L

$$\rho_{\mu\nu}^L(\varepsilon) = \sum_l c_{l\mu} c_{lv}^* \delta(\varepsilon - \varepsilon_l) \quad (1.119)$$

Therefore summation in (1.116) becomes integration

$$D_{\mu,v} = \int d\varepsilon \rho_{\mu\nu}^L(\varepsilon) n_F(\varepsilon_l - \mu_L) + \rho_{\mu\nu}^R(\varepsilon) n_F(\varepsilon_r - \mu_R) \quad (1.120)$$

Given that we are only interested in the scattering region (L-C-R), the coefficient $c_{l\mu}^0$ are zero for the basis functions (μ), therefore

$$c_{l\mu} = \sum_v [G(z)V]_{\mu v} c_{lv}^0 \quad (1.121)$$

So the spectral density matrix can be written as

$$\rho_{\mu\nu}^L(\varepsilon) = \left(G(\varepsilon) \frac{1}{\pi} \text{Im}[Vg^L(\varepsilon)V^\dagger] G^\dagger(\varepsilon) \right)_{\mu\nu} \quad (1.122)$$

Here we take use of the unperturbed left retarded Green's function

$$g_{\mu\nu}^L(\varepsilon) = \sum_l \frac{c_{l\mu}^0 c_{l\nu}^{0*}}{\varepsilon - \varepsilon_l + i\delta} \quad (1.123)$$

and with the relation

$$\{g_{\mu\nu}^L(\varepsilon) - [g_{\mu\nu}^L(\varepsilon)]^\dagger\}_{\mu\nu} = 2\pi i \sum_l c_{l\mu}^0 c_{l\nu}^{0*} \delta(\varepsilon - \varepsilon_l) \quad (1.124)$$

and that $g = g^T$ due to time-reversal symmetry.

We can finally express ρ^L as

$$\rho_{\mu\nu}^L = \frac{1}{\pi} [G(\varepsilon) \Gamma_L(\varepsilon) G^\dagger(\varepsilon)]_{\mu\nu} \quad (1.125)$$

where we use the definition of the retarded self-energy:

$$\Sigma^L(\varepsilon) \equiv [V g^L(\varepsilon) V^\dagger] \quad (1.126)$$

$$\Gamma_L(\varepsilon) \equiv i[\Sigma^L(\varepsilon) - \Sigma^L(\varepsilon)^\dagger]/2 \quad (1.127)$$

and a similar expression can be obtained for ρ^R

We can combine the left and right parts in (1.123)

$$G \Gamma G^\dagger = \frac{i}{2} G [\Sigma - \Sigma^\dagger] G^\dagger \quad (1.128)$$

$$= \frac{i}{2} G [(G)^{-1} - (G^\dagger)^{-1}] G^\dagger \quad (1.129)$$

$$= -Im[G] \quad (1.130)$$

where Σ consists of both Σ_L and Σ_R and time-reversal symmetry $G^\dagger = G^*$ was invoked.

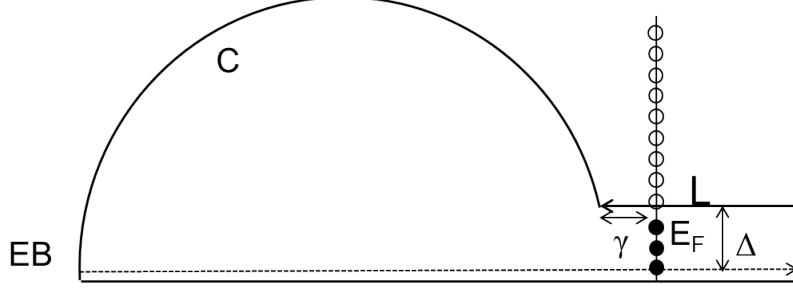


Figure 1.3: The closed complex contour consists of L $[\infty + i\Delta, EF - \gamma + i\Delta]$, C, and $[EB + i\delta, \infty + i\delta]$ enclosing the Fermi poles (black dots).

Now equation (1.123) reduces to a well-known expression

$$D = -\frac{1}{\pi} \int_{EB}^{\infty} d\varepsilon \text{Im}[G(\varepsilon)] n_F(\varepsilon - \mu) \quad (1.131)$$

$$= -\frac{1}{\pi} \text{Im} \left[\int_{EB}^{\infty} d\varepsilon G(\varepsilon) n_F(\varepsilon - \mu) \right] \quad (1.132)$$

As we can see from Figure 1.3, all the poles of the Green's function are lying on the real axis and the function is analytic otherwise. Instead of doing the integral on x-axis shown by the dotted line, we consider a contour defined for a given finite temperature shown by the solid line. The closed contour begins with a line segment L , followed by the circle segment C , and spans along the real axis from $(EB + i\delta)$ to $(\infty + i\delta)$ where EB is below the bottom valence-band edge. This contour only encloses poles originated from $n_F(z)$ located at $z_v = i(2v + 1)\pi kT$ with $x = E_F$. According to the residue theorem

$$\oint dz G(z) n_F(z - \mu) = 2\pi i kT \sum_{z_v} G(z_v) \quad (1.133)$$

therefore the overall contour integration is

$$\int_{EB}^{\infty} d\varepsilon G(\varepsilon) n_F(\varepsilon - \mu) = - \int_{C+L} dz G(z) n_F(z - \mu) - 2\pi i k T \sum_{z_v} G(z_v) \quad (1.134)$$

The contour integral can be computed numerically using a given finite temperature by choosing the number of Fermi poles to enclose. This insures the contour stays away from the real axis to avoid singularities and therefore the Green's function behaves sufficiently smooth.

1.5.4 Procedure for calculating Nonequilibrium density matrix and potential

When source-drain bias is presented, the density matrix consists of the equilibrium part $D_{\mu,v}^L$ and the Nonequilibrium part $\Delta_{\mu,v}^L$:

$$D_{\mu,v} = \int d\varepsilon \rho_{\mu v}^L(\varepsilon) n_F(\varepsilon_l - \mu_L) + \rho_{\mu v}^R(\varepsilon) n_F(\varepsilon_r - \mu_R) \quad (1.135)$$

$$= D_{\mu,v}^L + \Delta_{\mu,v}^R \quad (1.136)$$

where

$$D_{\mu,v}^L = -\frac{1}{\pi} \text{Im} \left[\int_{EB}^{\infty} d\varepsilon G(\varepsilon) n_F(\varepsilon - \mu_L) \right] \quad (1.137)$$

and

$$\Delta_{\mu,v}^R = \int_{EB}^{\infty} d\varepsilon \rho_{\mu v}^R(\varepsilon) [n_F(\varepsilon - \mu_R) - n_F(\varepsilon - \mu_L)] \quad (1.138)$$

or equivalently

$$D_{\mu,v} = \int d\varepsilon \rho_{\mu v}^L(\varepsilon) n_F(\varepsilon_l - \mu_L) + \rho_{\mu v}^R(\varepsilon) n_F(\varepsilon_r - \mu_R) \quad (1.139)$$

$$= D_{\mu,v}^R + \Delta_{\mu,v}^L \quad (1.140)$$

where

$$D_{\mu,v}^R = -\frac{1}{\pi} \text{Im} \left[\int_{EB}^{\infty} d\varepsilon G(\varepsilon) n_F(\varepsilon - \mu_R) \right] \quad (1.141)$$

and

$$\Delta_{\mu,v}^L = \int_{EB}^{\infty} d\varepsilon \rho_{\mu v}^R(\varepsilon) [n_F(\varepsilon - \mu_L) - n_F(\varepsilon - \mu_R)] \quad (1.142)$$

We notice that only the "equilibrium" part of the density matrix is real due to the time-reversal symmetry. The "Nonequilibrium" part cannot be made real since it breaks the time-reversal symmetry by the scattering states. However, we can neglect the imaginary part of D , if we are only interested in the electron density:

$$n(\vec{r}) = \sum_{\mu,v} \phi_{\mu}(\vec{r}) [D_{\mu v}] \phi_v(\vec{r}) \quad (1.143)$$

Since we can the charge density from the density matrix which is obtained using Green's function, we can again construct Hamiltonian. The DFT effective potential consists of three parts: Pseudopotential V_{ps} , the exchange correlation potential V_{xc} , and the Hartree potential V_H . The Hartree potential can be determined by solving Poisson's equation:

$$\nabla^2 V_H(\vec{r}) = -4\pi n(\vec{r}) \quad (1.144)$$

Suppose $\phi(r)$ is a solution of the Poisson equation, then the general solution is:

$$V_H(\vec{r}) = \phi(\vec{r}) + \vec{a} \cdot \vec{r} + b \quad (1.145)$$

The remaining two parameters a_x and b can be determined by the value of potential at the $L-C$ and $C-R$ boundaries. The electrostatic potential in the L and R region can be determined from separate bulk calculations and then shifted relative to the source-drain bias. Therefore, the Hartree potential can be uniquely determined iteratively with these boundary conditions.

1.6 Molecular Dynamics simulation

Molecular dynamics (MD) is a simulation process of physical movements of atoms and molecules in a system with well defined boundary conditions. The atoms and molecules are allowed to interact, giving us a clear view of the motion of the system for a period of time. The trajectories of the atoms and molecules are determined numerically by solving the Newton's equations of motion. Forces between the particles and the potential energy are evaluated by molecular mechanics force fields.

Because most molecular systems of interests consist of a huge number of particles, it is often impossible to find the properties of such complex systems analytically. MD simulation can solve this problem by using numerical methods. However, long MD simulations are mathematically ill-conditioned due to cumulative errors in numerical integration. The error can be controlled by proper selection of algorithms and parameters, but cannot be eliminated entirely.

The MD method is widely applied today in the field of materials science, biochem-

istry and biophysics. For instance, it is frequently used to simulate three-dimensional structures of proteins and other macromolecules based on experimental constraints from X-ray crystallography or NMR spectroscopy. Moreover, MD is often used to examine the dynamics of atomic-level phenomena that cannot be observed directly, such as protein folding and metalloprotein chelation in Alzheimer’s disease [77]. It also plays an important role on examining the physical properties of nanotechnological devices that are really difficult to understand without the details of their dynamical conformations.

The classical force field used for the molecular dynamical simulation represents the real effective force acting on a particle. All particles in the system are described using the particles’ locations, velocities and acceleration. The relative displacement of two particles, r_{ij} , is the positional metric for determining the force interaction between the them. Thus the total force applied to any particle i can be obtained by summing over all forces exerted from other particles. In practice it is often easier to first obtain the total potential for each particle in the form of a scalar field, reducing the computation overhead of vector sums. The force on any particle i is then computed as the negative gradient of the total potential at the position of particle i .

Let’s briefly introduce an implementation of the molecular dynamics algorithm using classical force field.

1. For each atom, determine the effective total potential as the sum of potential produced from all other interacting atoms

$$V_i = \sum_{j \neq i} v_j(r_{ij}) \tag{1.146}$$

2. For each atom, determine the total force by calculating the negative gradient of the

total potential at the location of the atom

$$\mathbf{F}_i = -\nabla V(r_i) \quad (1.147)$$

3. Update the positions and the velocities after a small time step for each atom

$$r'_i = r_i + \left[\frac{p_i}{m_i} + \frac{\mathbf{F}_i}{2m_i} \Delta t \right] \Delta t \quad (1.148)$$

$$p'_i = p_i + F_i \Delta t \quad (1.149)$$

4. Repeat from step 1 until the simulation reach to a certain period of time and the desired physical properties of the system can be obtained from the dynamical trajectory.

A molecular dynamics simulation should also account for the available computational power. On one hand, the number of particles, time step and total time duration must be carefully selected so that the calculation can finish within a reasonable time period. On the other hand, the simulations should be long enough to reach the time scales of the natural processes being studied. To make statistically valid conclusions from the simulations, the time span should match the kinetics of the natural process. Many scientific publications regarding to the dynamics of proteins and DNA use data from simulations spanning several nanoseconds to microseconds depending on different process. To obtain these simulations, parallel algorithms allowing the load to be equally distributed in CPUs are used.

During a classical MD simulation, the most intensive task is the evaluation of the

force field potential as a function of the particles' coordinates. For energy evaluation, the most expensive part is the non-bonded interaction which scales by $O(n^2)$ if all pairwise electrostatic and van der Waals interactions must be evaluated explicitly. However, this huge computational cost can be reduced to $O(n\log(n))$ by employing electrostatics methods such as Particle Mesh Ewald (PME). With the help of a very fast computational method, namely, fast Fourier transformation, PME is a useful method for dealing with long range electrostatic interactions in the system when periodic boundary conditions are present. The particle mesh is a 3-D grid over which the system charge is distributed. Therefore, the grid size should be chosen such that it is fine enough to accurately represent the system. Usually, the number of grid points should be greater than or equal to length of the basis vector.

1.6.1 CHARMM Force Field

CHARMM force field is one of the implementation of force field potentials. There are several versions of the CHARMM force field available. For instance, CHARMM22 [52] and CHARMM27 [53, 18] are the two most popular versions of the force field. For protein systems, the two are equivalent. However, CHARMM27 has been optimized for simulating DNA, RNA, and lipids. Using CHARMM force field, NAMD package [70] allows generation and analysis of a wide range of molecular simulations. Minimization of a given structure and simulation runs of a molecular dynamics trajectory are the two basic kinds of simulations. More advanced features include free energy perturbation (FEP), quasi-harmonic entropy estimation, correlation analysis and combined quantum, and molecular mechanics (QM/MM) methods.

The CHARMM force field consists six terms in the potential energy function. For the

remainder of the CHARMM discussion we will explain each term.

$$\begin{aligned}
V(r) = & \sum_{\text{bonds}} K_b(b - b_0)^2 + \sum_{\text{angles}} K_\theta(\theta - \theta_0)^2 + \sum_{\text{dihedrals}} K_\phi(1 + \cos(n\phi - \delta)) \\
& + \sum_{\text{impropers}} K_\omega(\omega - \omega_0)^2 + \sum_{\text{Urey-Bradley}} K_{UB}(S - S_0)^2 \quad (1.150) \\
& + \sum_{\text{nonbonded}} \left(\varepsilon \left[\left(\frac{\rho_{ij}}{r_{ij}} \right)^{12} - \left(\frac{\rho_{ij}}{r_{ij}} \right)^6 \right] + \frac{q_i q_j}{\varepsilon r_{ij}} \right)
\end{aligned}$$

The first term is based on the harmonic inter-atomic displacement metric. It accounts for the bond stretches. k_b is the bond force constant and b_0 represents the relaxed bond length at equilibrium. $b - b_0$ represents the displacements from equilibrium that the atom has moved from. The second term in the equation accounts for the bond angles between two neighbour bonds. k_θ is the angle force constant and $\theta - \theta_0$ is the angle from equilibrium positions of the two neighbour bonds. The third term is for the dihedrals where k_ϕ refers to the dihedral force constant, n is the multiplicity of the function, ϕ is the equilibrium dihedral angle and δ is the phase shift. The fourth term represents the impropers, which refers to the out of plane bending. k_ω is the force constant and $\omega - \omega_0$ is the out of plane angle. The Urey-Bradley component accounting for angle bending is represented in the fifth term, where k_{UB} is the respective force constant and S is the distance between the 1,3 atoms in the harmonic potential.

The nonbonded interactions between any pair of atoms, for instance (i, j) , are represented by the last term. The nonbonded forces are only applied to atom pairs which are separated by at least three bonds. The van Der Waals (VDW) energy is evaluated using a standard Lennard-Jones potential. The electrostatic energy with a Coulombic potential is also included. In the Lennard-Jones potential above, the ρ_{ij} is where the Lennard-Jones

potential is zero. In order to run the MD simulations, the parameter file must have all the terms specified in the energy function.

Chapter 2

Introduction

In this chapter, we briefly introduce the subject of DNA, including its basic geometric structure, the composition of double stranded molecule and its general electronic properties.

2.1 Introduction to DNA

Deoxyribonucleic acid (DNA) was first discovered by James Watson and Francis Crick in the early 1950s. It is a molecule which encodes the genetic instructions. Along with RNA and proteins, DNA is one of the three major molecules essential for life. We are now in such an exciting time with the rise of molecular biology. Its many offspring are likely to reshape nearly every aspect of contemporary life. With the completion of the first draft of the human genome sequence trumpeting the beginning of the twenty first century, success in the biological sciences is occupying the center stage, linking the biological science to chemical, physical, mathematical and computer sciences.

The genetic information is encoded as a sequence of nucleotides (guanine, adenine,

thymine, and cytosine) represented with the letters G, A, T, and C. Most DNA molecules are double-stranded helices, consisting of two long polymers. The backbones are made of alternating sugars (deoxyribose) and phosphate groups (related to phosphoric acid), with the nucleobases (G, A, T, C) attached to the sugars. The bases are classified into two types. The purines, A and G, being fused five- and six-membered heterocyclic compounds, are also called as double-ring bases. The pyrimidines, the six-membered rings C and T are also called as single-ring bases.

The two strands run in anti-parallel direction, with one strand being 3' (three prime) end and the other strand being 5' (five prime) end at the same side. As shown in Figure 2.1, this refers to the direction the 3rd and 5th carbon on the sugar molecule. Attached to each sugar is one of four types of molecules called nucleobases (we will refer them as bases). It is the sequence of these four bases along the backbone that encodes information. DNA chain is measured to be 22 to 26 angstroms wide, and one nucleotide unit is measured to be 0.34 nm long. Although each individual repeating unit is very small, DNA polymers can be very large molecules containing many of nucleotides.

The DNA double helix is stabilized by two major forces: hydrogen bonds within a base pair and base-stacking interactions between aromatic intrastrand neighbor bases. As hydrogen bonds are not covalent, they can be broken and rejoined easily. The two strands of DNA in a double helix can therefore be unpaired like a zipper, either by a mechanical force or high temperature. The conjugated π bonds of nucleotide bases align perpendicularly to the axis of the DNA molecule due to base-stacking interactions.

DNA exists in many possible conformations, such as A-DNA, B-DNA, and Z-DNA. The conformation that DNA adopts depends on the hydration level, DNA sequence, the amount and direction of supercoiling, chemical modifications of the bases, the type and concentration of metal ions, as well as the presence of polyamines in solution. B-DNA is

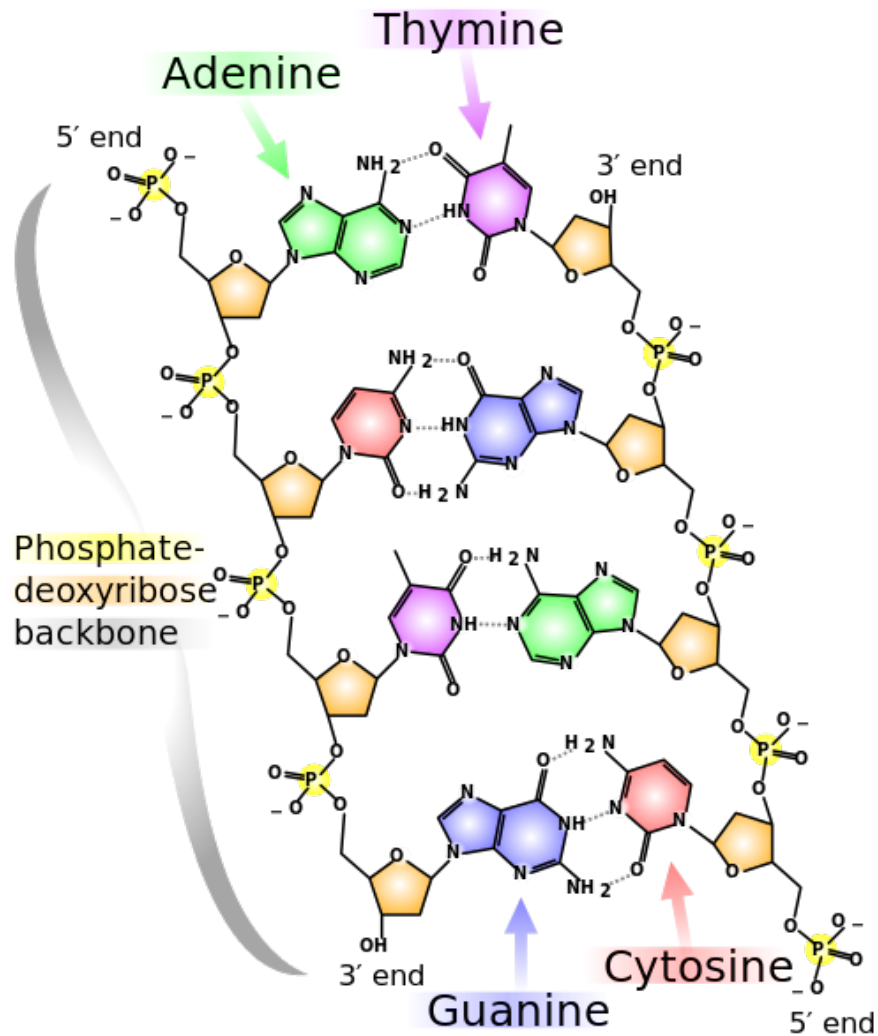


Figure 2.1: DNA chemical structure. The two strands of double helical DNA have opposite directions, one going from the 5' end to the 3' end, the other from the 3' end to the 5' end. The number 3' and 5' refer to the position of carbon in deoxyribose. Guanine (G) usually paired with cytosine (C) by three hydrogen bonds (shown as dotted lines); adenine (A) usually paired with thymine (T) by two hydrogen bonds. Negatively charged phosphate backbones consists of alternating phosphate groups and sugar rings. Figure retrieved from http://en.wikipedia.org/wiki/File:DNA_chemical_structure.svg

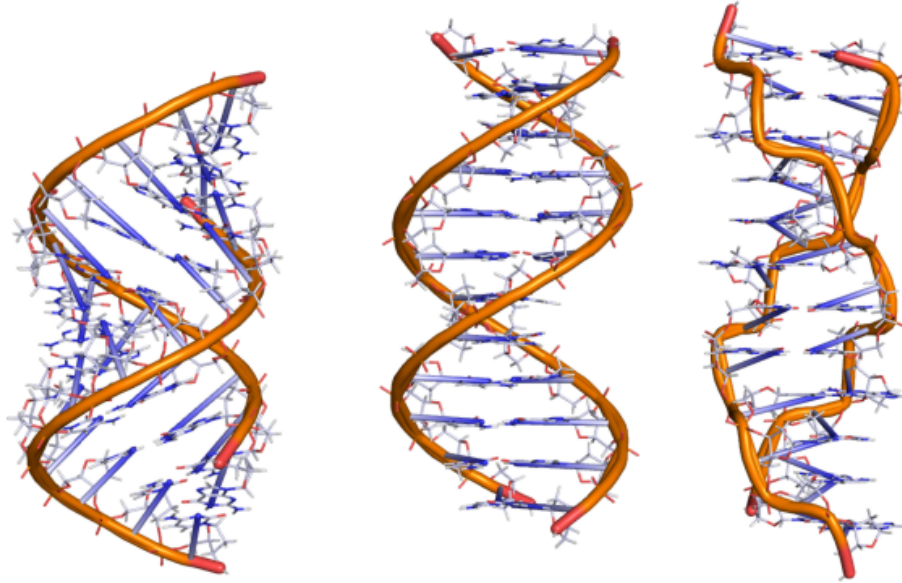


Figure 2.2: The structures of A (left), B (middle) and Z (right) DNA. DNA structures built from 3DNA [51].

the most common under the conditions found in cells. Compared to B-DNA, the A-DNA is a wider right-handed spiral, with a shallow, wide minor groove and a narrower, deeper major groove. Z-DNA is a left-handed double helical structure which winds to the left in a zig-zag pattern as shown in Figure 2.2. The corresponding geometry attributes are listed in Table 2.1

2.2 Motivation of using DNA as an electronic material

The principal story of DNA has long centered on the fundamental role in carrying the genetic code of organisms. However, there has been a lot of interest in its electronic properties recently, motivated by its potential biological and technological applications.

Table 2.1: Geometry attribute of different forms of DNA

Geometry attribute	A-form	B-form	Z-form
Helix sense	right-handed	right-handed	left-handed
Rotation/bp	33.6°	35.9°	60°/2
Rise/bp	2.4 Å	3.4 Å	3.7 Å
Mean propeller twist	+18°	+16°	0°
Diameter	23 Å	20 Å	18 Å

The highly specific binding between the two strands of DNA, its ability to synthesize DNA in any molecular sequence makes it a natural candidate for use in molecular electronics industry.

As early as 1962, Eley and Spivey suggested that the interbase hybridization of the π_z orbitals along the axis of DNA could lead to a delocalized state and therefore lead to conducting behavior. There are also similar stacked aromatic crystals that are indeed metallic, such as the famous Bechgaard salts [78]. However, there are also crucial differences between DNA and the conventional conductors. One of the most significant differences is that DNA is not a periodic system. DNA is also greatly under the influence of its environment, such as the water molecules and counterions surrounding the DNA. The double helix of DNA acts to keep the hydrophobic bases out of the water, but the negatively-charged phosphate group on the backbone requires positive counterions to shield its potential. The water molecules and counterions exert non-negligible potential on the electrons in the base pair stack, and therefore contribute to the random electronic environment. The dielectric medium provides a fluctuating potential for the local DNA segment.

In addition, the lowest ionization potential (IP) of guanine is about 0.2 eV lower

than adenine and 0.6 eV lower than cytosine and thymine bases [30]. The difference of IP between the pyrimidine and purine bases is higher than the estimated electronic coupling between the highest occupied (HOMO) or lowest unoccupied molecular orbitals (LUMO) of the neighboring bases. This leads to the expectation of localization of the electronic state.

DNA itself is very flexible at the room temperature, giving the potential possibility of replication or partial uncoiling. Therefore, conformational change of its structure is also an important factor in determining its electronic properties.

2.3 DNA as a molecular wire in molecular electronics

Interesting hints began to merge twenty years ago in the studies of Barton and co-workers, who observed distance-independent charge transfer between DNA-intercalated transition-metal complexes [59] and noted its implications in biotechnology. For example, they demonstrated photoinduced oxidation by a rhodium metallointercalator in DNA over 40 angstrom away within 0.1 nano-second(ns).[28] Another experiment showed that thymine dimer could be healed by a photoexcited rhodium intercalator molecule from 16 base pairs away.[12]

Barton and coworkers have hypothesized that there could be signal and receiver protein exploiting the electron migration properties of DNA. In the absence of damage, DNA could be probed electronically and the receiver protein could be reduced and detached by electron transfer. It should be noticed that while the transfer can be rapid, very long range migration could be much slower due to multiple hops. But this process is still very

fast in a sense that cell replication in an organism usually takes about a day.

In the past 15 years, there have been many experimental studies of DNA's conductance, leading to a wide range of results. It is of tremendous importance to resolve these issues, given that electron transport in DNA could have a variety of applications in molecular electronics and biotechnology. For example, a DNA chip could be used for DNA sequencing, disease screening, and gene expression analysis. If DNA can conduct sufficiently well, a sequence could be read out electronically instead of visually with the fluorescent dyes. The general idea is that floppy single strands of DNA are insulating, but well-stacked double stranded DNA after successful hybridization could be conducting.

In addition, DNA's sequence-dependent self-assembly properties could be taken advantage of to build complex nanowire arrangements. Interesting topological structures could be created with DNA by Seeman and co-workers.[10] DNA-based templating may also have important applications in nanoelectronics. The sticky ends at the ends of the helix can be used to attach single DNA molecules to modified metal electrodes, bypassing the need for precise nanofabrication and mechanical manipulation, therefore solving the difficulties in precise localization and interconnection of nanotubes. [8] [74] Moreover, the first single-DNA field transistor was built by Kawai's group [91] using the intrinsic conducting properties of short DNA segments.

2.4 DNA sensors: capable of detecting mutations and disease

DNA sensors are known to be useful for genomic sequencing and mutation detection. Although sophisticated techniques to assay the hybridization of DNA target sequence with

arrays of immobilized single stranded DNA have been developed for genomic sequencing and mutation detection, hybridization assays are inherently limited in sensitivity when it comes to base-mismatch detection. Detection of a point mutation requires a distinguishable difference in pairing energy. The difference therefore is often too small to be measurable. As a consequence, detection of point mutation requires extensive manipulation of hybridization conditions and sophisticated deconvolution algorithms.

Monitoring charge transport through DNA helix provides an alternative way for the detection of point mutations. DNA-mediated charge transport shows a weak distance dependence but is extremely sensitive to perturbations in the base stack: intervening bulges prevent long-range photochemical guanine oxidization [27], and single-base mismatches remarkably reduce the electron transfer yields [42]. Barton and coworkers have shown that a deliberately induced damage to DNA can greatly reduce electron migration [43, 41] and DNA conductivity [26]. Therefore, DNA-mediated charge transport may provide a signaling mechanism for DNA-based sensors.

Chapter 3

First-principles studies of conformation and solution effects on DNA transport

3.1 Introduction

Charge transport (CT) along the helical axis of DNA has received considerable attention by researchers over the past 20 years due to potential applications in bio/nano-electronics [73, 26, 63], electrochemical DNA sequencing [57] and design of nanoscale sensors for detection of DNA mutations or protein binding to DNA [81]. In addition, CT in DNA has a biological function as it plays an important role in the process of DNA repair [6]. Numerous experimental studies of CT in DNA have yielded a wide range of conflicting results, ranging from insulating [13, 92], semiconducting [72], metallic [91] and even superconducting [39]. This is because DNA conductivity is sensitive to many factors such as contacts with electrodes, coupling between the DNA base pairs, DNA length

and sequence, thermally induced motion, and interaction with solvent and counterions. However, studies that utilized well-defined DNA contacts and preserved the native conformation in buffered solution, have achieved more consistent results with conductivities between $10^{-5}G_0$ and $10^{-2}G_0$ [59, 41, 11, 35, 90, 26], G_0 being $2e^2/h$. For example, Guo *et al.* used a single DNA molecule connected to carbon nanotube leads [26]. Results showed that a well-matched 15-base-pair B-DNA has a conductance of about $10^{-2}G_0$ with a source-drain bias of 50 mV while a mismatch led to a dramatic decrease of the conductance.

Traditionally, charge transport in DNA has been explained in terms of two processes called superexchange and hopping. The former is a single step process, in which a hole tunnels directly from a donor to an acceptor without occupying the intervening base pairs [38, 23, 20, 24]. Superexchange transport decays exponentially with relatively large decay constant and thus is only relevant for distances of only a few base pairs. To explain long distance transport along DNA, hopping mechanism has been proposed. This process consists of multiple superexchange steps with holes being briefly localized on either guanines [21] or adenines [22] and then "hop" onto nearby bases via superexchange. Hopping has shallower distance dependence because it avoids long tunneling steps. Other types of transport have also been described. For example, Barton and coworkers observed a single-step charge transport mechanism overtaking hopping at longer distances [20]. In contrast to superexchange, charge is delocalized over the intermediate bases pairs.

Theoretical studies of CT in DNA have been performed at various levels of accuracy including *ab initio* [67, 55, 54] and semiempirical methods [30, 47, 82, 25, 75]. At an *ab initio* level, NEGF/DFT methodology was employed. Due to the high computational cost, studies have been limited to a single DNA conformation considering either a canonical DNA structure or a snapshot obtained from classical molecular dynamics. Sanvito

and coworkers investigated the conductance of an ideal dry 6-base pair A-DNA connected to gold leads. They found conductance values ranging from $10^{-13}G_0$ to $10^{-16}G_0$, which is several orders of magnitude smaller than that observed in experiments [67]. They also concluded that adding solvation decreases the transport. Maeda *et al.* studied a 4-base pair CGCG B-DNA snapshot connected to gold leads. They considered both dry and hydrated cases and found that hydration enhances the current by an order of magnitude at the gate bias of 0.3 V [54]. Mallajosyula *et al.* investigated the sequence dependence of electron transport in wet DNA [55]. Their calculation used a single structure averaged from 10 snapshots sampled over 1 ns MD simulation. They found a delocalized orbital extending over several guanine sites but not over the whole DNA molecule.

Many semiempirical studies on CT in DNA exist in literature. Their advantage over *ab initio* works is that they can consider longer DNA and/or more conformations to better describe thermal motions. For example, Hatcher *et al.* investigated the electronic coupling between donor and acceptor in DNA and PNA using thousands of MD snapshots. Their model only included base pairs, while DNA backbones, water and counterions were excluded [30]. They found that the coupling fluctuates considerably and that peptide nucleic acid (PNA) has a larger coupling compared to DNA due to bigger geometric overlap between neighboring bases and a larger structural flexibility. Similarly, Troisi and Orlandi also found that the effective coupling fluctuates greatly over the MD simulation. They identified the transverse motions of the DNA bases as the main factor determining the couplings [82]. Lee *et al.* [47] attempted to explain results of experiments by Guo *et al.* [26], in which a dramatic difference in CT between well matched and mismatched cases was observed. Of the two models used, only one was able to reproduce the experimental results and even then an appropriate value of Fermi energy had to be used. They also found that the degree of charge localization onto the backbones can be strongly affected

by the theory level, becoming weaker when using an *ab initio* approach.

In this work, we perform extensive DFT/NEGF calculations to gain new insight into CT in DNA. We investigate multiple snapshots extracted from MD trajectories to determine the how solvent, counterions, DNA conformation and sequence affect the CT. The results show that while both solvent and counter ions modulate the conductivity, the main factor is DNA conformation. We also find that while the optimum structure is preferred for CT along the poly(G)-poly(C) chain, this is not the case for other sequences. This chapter is organized as follows. Section 3.2 describes the methodology we use for classical MD simulations and quantum calculations of transmission using Landauer formula and Green's function formalism. In Section 3.3, we show the calculated results with the discussion focused on the effect of counterions, water molecules, DNA conformations and DNA sequence including mismatched DNA. Lastly, we summarize our conclusions in section 3.4.

3.2 Methodology

Our calculations consider a B-DNA connected to (5,5) carbon nanotube (CNT) leads via alkane linkers $CONH - (CH_2)_3$. The system is first investigated in molecular mechanics(MM) calculations using NAMD [70] with CHARMM27 [17] force field. A simulation box of dimensions $160 \times 160 \times 160 \text{\AA}^3$ is considered and periodic boundary conditions are applied. Particle Mesh Ewald (PME) procedure is used to account for the long-range interactions. The system is solvated by adding two thousand water molecules around DNA. Na^+ and Cl^- ions are added to balance DNA charged backbones and achieve saline concentration of 0.05 mol/L. MM calculations start with equilibration for 0.1 ns, after which the calculation is continued for additional 2ns, during which 20 snapshots are

recorded.

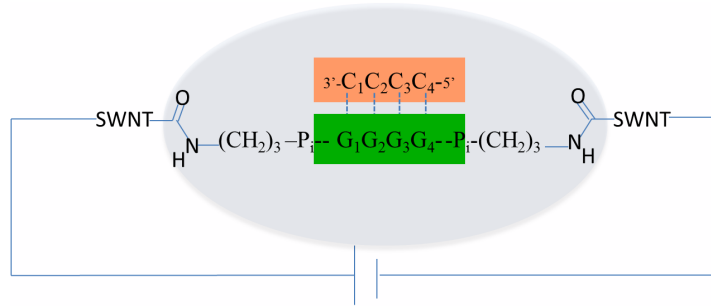


Figure 3.1: The configuration of 4BP poly(G)-poly(C) DNA sandwiched between SWNT. The shaded area represents the solvent environment.

Transport properties of the MM snapshots are analyzed at quantum level using non-equilibrium Green function (NEGF) technique as implemented in our localized orbital density functional theory(DFT) code [16, 60, 50]. The quantum calculations include CNT leads, linkers, DNA and a first solvation shell, which is defined as water molecules and counterions within 3\AA of the DNA. The rest of water molecules and counterions are omitted. The total charge of the omitted counterions is treated as a uniform charged background.

The setup for such a quantum calculation of a 4BP poly(G)-poly(C) DNA is shown in Figure 3.1. Six orbitals per atom with a cutoff radius of 9 Bohr were used in the localized orbital calculations. The electron-ion interactions are represented by ultrasoft pseudopotentials [36, 84]. The implementation is based on RMG [9, 36, 4] code in which Kohn-Sham equations are solved in real-space and the multigrid technique is used to accelerate convergence of the ground state wavefunctions. The Hamiltonian and the Green's function are obtained self-consistently from DFT calculation with complex contour integration [7]. The potentials and charge densities of the leads are fixed to those corresponding to

the bulk material. The effects of the infinite CNTs are included in the self-energy terms of the left (L) and right (R) leads. Eight atomic layers of CNT are included at both sides of the central conductor (C) to account for screening effects so that the potentials and the charge densities match at the interfaces between the conductor and leads after self-consistent iterations. The Hartree potential is obtained by solving Poisson's equation with boundary conditions matching the potentials of all the leads. After the KS potential and the charge density are obtained self-consistently, we calculate the transmission coefficient using the Landauer formula.

$$T(E) = Tr[\Gamma_L(E)G_C^R(E)\Gamma_R(E)G_C^A(E)] \quad (3.1)$$

where Γ_L , Γ_R and G_C^R , G_C^A are the coupling functions for the left and right leads and retarded and advanced Green's functions of the conductor part, respectively. The current is obtained by integrating the transmission curve over the HOMO band below the Fermi level using a source-drain bias of $V_{sd} = 50mV$ [26], and multiplied by $G_0 = 2e^2/h$.

$$I = \frac{2e^2}{h} \int_{-V_{sd}}^0 T(E)dE \quad (3.2)$$

Automatic enhancement of the energy grid is implemented to integrate transmission curves with sharp peaks. The technical details are presented in the Appendix. It has been argued that self-interaction correction (SIC) is fundamental to obtain a proper molecular-level alignment [67]. We do not consider the SIC since the current is obtained by integrating the HOMO band which is pinned to the Fermi level of the leads [55].

3.3 Results and discussion

3.3.1 Thermal Fluctuations in DNA Conductivity

DNA is highly flexible at room temperature. To capture the effect of thermal fluctuations we extract 20 snapshots from a 2 ns molecular mechanics simulation of fully solvated DNA. Our NEGF calculations include the DNA, the solvent and the counterions in the first solvation shell. We first consider 4BP and 10BP GC DNA. We choose GC base pairs because they provide good conductivity due to guanine’s low ionization potential [46] and high hole mobility [3, 48, 85, 44]. Hydrogen bonding between G and C is stronger than that in A-T base pairs. One expects, from simple orbital mixing arguments, that the poly(G)-poly(C) homogeneous sequence should display fast charge transfer properties. The calculated currents for both 4BP and 10BP cases are displayed as histograms in Figures 3.2. The conductivities vary over several orders of magnitude: from 10^{-7} nA up to 10^{-1} nA for 4BP and from 10^{-14} nA up to 10^{-2} nA for 10BP DNA. The average is 0.1 nA for the 4BP DNA and 0.0029 nA for the 10BP DNA. Assuming exponential length dependence of the current, $I(L) = I_0 \exp(-\beta L)$, which is often assumed for DNA [5], the value of the decay constant β can be estimated as 0.18\AA^{-1} . This weak distance dependence is consistent with experimental findings by O’Neill and Barton [64], but it should be noted that previous works have obtained a wide range of β values from 0.05\AA^{-1} to 1\AA^{-1} [80, 90, 15, 58]. Next, we explore the cause behind the large variance of current between snapshots taken from MD simulations. In our setup, four factors influence the conductance: DNA structure, linker structure, solvent configuration, and counterion positions. In the following we examine each of those independently to gauge their importance.

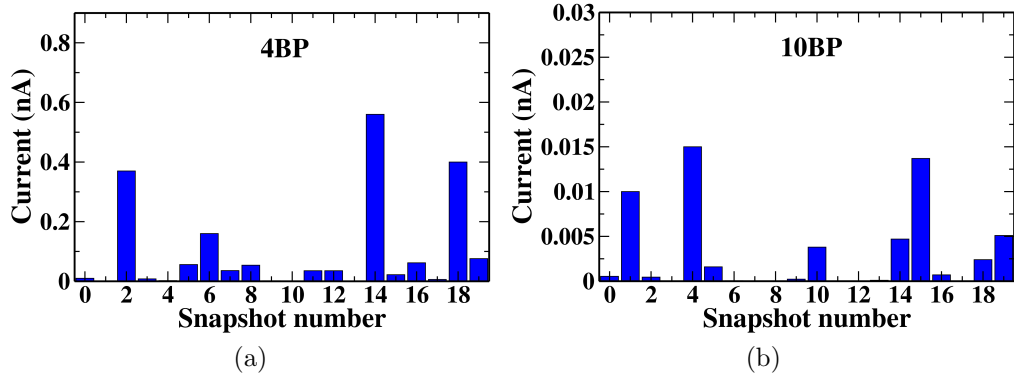


Figure 3.2: Histogram of calculated current for 4BP and 10BP poly(G)-poly(C) DNA

Linker Thermal Motion

The alkane linker used in our calculations is insulating with a large band gap [40] and thus suppresses the overall current. It has been shown [40] that the resistance of an alkane wire roughly scales as $R = R_0 \exp(\beta_{alkane} \cdot n)$, where n is the number of carbon atoms and $\beta_{alkane} \approx 1$. In our calculations, $n = 8$ and thus the linker is expected to decrease the current by a factor of about 3000. While this is a large suppression, here we are concerned with how much it changes between MD snapshots. The linker structure changes during MD simulations and thus linker may be a factor causing large differences in current. To examine this, we have set up a restrained MD simulation of 4BP DNA with the alkane linker kept frozen. 10 snapshots were extracted from this simulation and the currents were calculated in the same way as for a fully flexible DNA system. We find that the average current is similar (0.13 nA) as in the fully flexible case and that ratio between the maximum and the minimum currents is six orders of magnitude as before. Therefore, we conclude that the linker flexibility does not influence DNA conductivity significantly. The carbon-carbon single bond linkers are standard in experimental setups, however, one cannot completely rule out the possibilities that some parts of the DNA

have direct contacts with the electrodes, thus reducing the contact resistance as discussed in Ref.[67].

Role of counterions in DNA conductivity

To investigate how much of the current variation is caused by counterions, we repeat the 4BP NEGF calculations with counterions removed. The charge state of all snapshots is -8 and this is accounted for by using uniformly charged background. The calculated currents are shown in a histogram in Figure 3.3. The results show that after removal of the ions the average current increases by a factor of two to 0.205 nA, while the minimum and maximum are 3×10^{-5} nA and 1.4 nA, respectively. Thus, while the presence of counterions decreases DNA conductivity, their dynamics is not an important factor behind the large variation of current passed through DNA.

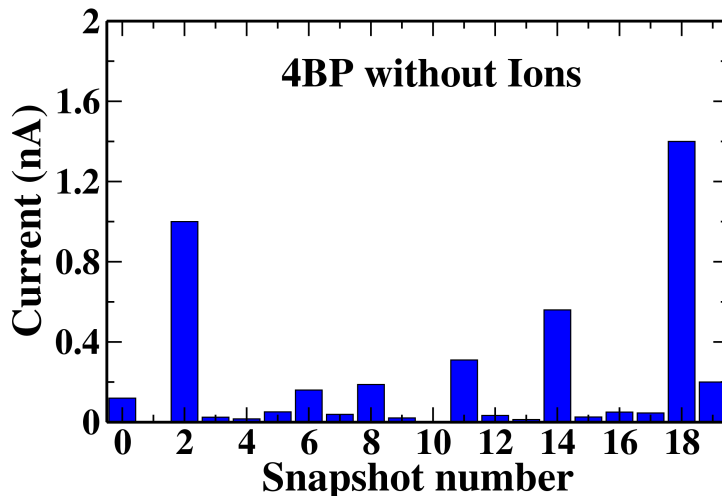


Figure 3.3: Histogram of calculated current of 4BP poly(G)-poly(C) DNA without explicit counterions.

To investigate the effects of counterions, we further analyze several snapshots with

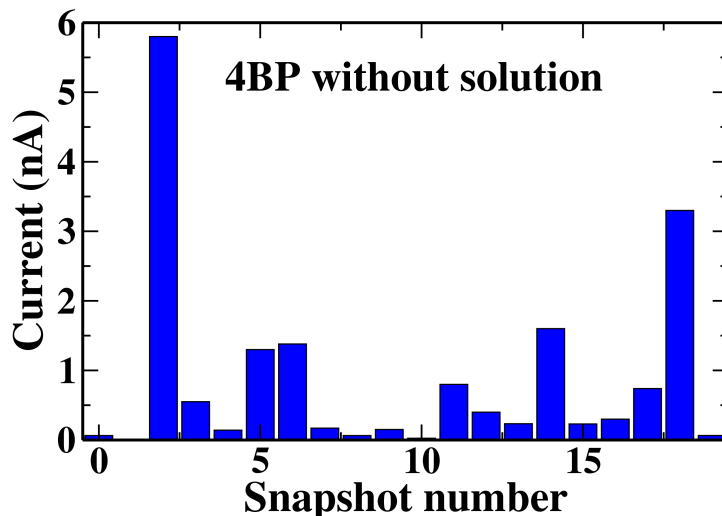


Figure 3.4: Histogram of calculated current of 4BP poly(G)-poly(C) DNA without surrounding water molecules

the highest conductivities when counterions are present. This can be best demonstrated for snapshot 2, which is visualized in the right panel in Figure 3.5(a). This snapshot contains two counterions in the DNA vicinity. One of them is near the phosphate group connecting G2 and G3, while the other one is close to G4. The transmission curve for this configuration is shown in the left panel in Figure 3.5a. (Only the channels below the Fermi level are shown because the conductivity is dominated by hole transfer.) Analysis of the conducting states near the Fermi level shows that in contrast to other guanines, no states are significantly localized on G4. (See HOMO-2 in Figure 3.5(a) for an example) This is caused by the counterion near G4, because when this ion is omitted from the snapshot, the conductive states are extended over all guanines as shown in Figure 3.5(c). In previous studies, Barnett *et al.* [2] also investigated ion-gated transport and found that hole states characterized by varying degrees of localization are governed by an evolving ionic configurations. It should be noted that the current between different ionic configurations can be calculated and compared directly in our work. For instance, the

current increases by a factor of 3 after removal of the counterion near G4. Closeness to a guanine is the critical factor because when the second ion, which is not in the vicinity of a guanine, is removed, no changes in the current and transmission spectrum are observed as shown in Figure 3.5(b). This behavior is true for other snapshots that we analyzed in the same way. Thus we conclude that counterions close to guanine bases decrease the conductivity of DNA by blocking conducting states from occupying the guanines. This is most likely due to electrostatic interaction between positive ions and a charge on a guanine, causing an energy shift of the states located there, away from the HOMO energy region. The influence of counterions on conductivity is location-dependent, because counterions near the phosphate groups do not play a role in DNA CT.

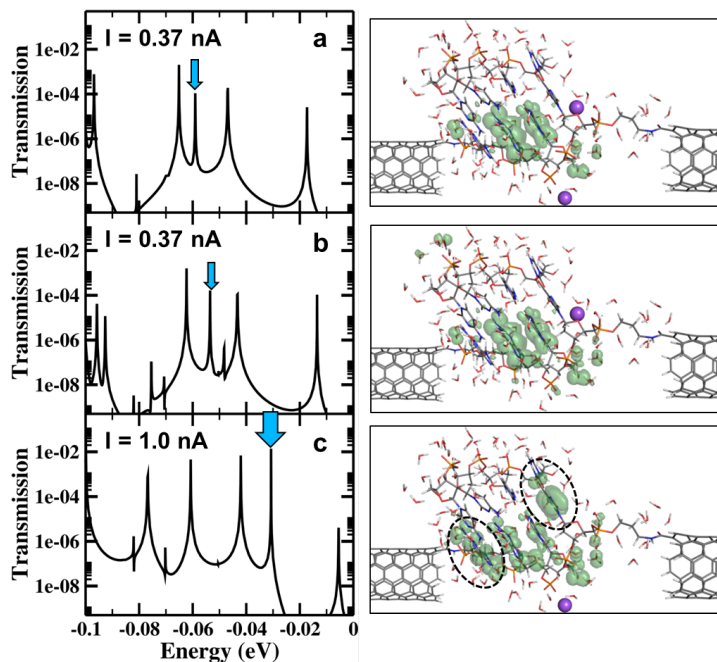


Figure 3.5: Calculated transmission curves (left panels) and local density of states (right panels) for (a) both counterions present, (b) counterion near the phosphate group removed, (c) counterion near G4 removed. Positive counterions are shown as purple spheres. The isosurface in the right panel corresponds to the peak labeled by the blue arrow on the left panel. Dash-circled regions indicate more extended state.

Role of water molecules in DNA conductivity

To isolate the role of solvent, we compare conductivity through 4BP DNA with and without the first shell of water, as shown in Figures 3.3 and 3.4, respectively. In both cases, counterions were not present. The comparison shows that water presence decreases the current by a factor of four on average, from 0.86 nA (without water) to 0.205 nA (with water). The ratio between the maximum and minimum increases from 10^4 (without water) to 10^5 (with water) and thus solvent dynamics is not the main reason for large fluctuations in DNA current. It should be noted that these calculations are computational experiments designed to investigate the role of water and not an accurate representation of a real DNA. In fact, water removal would cause structural changes in DNA. B-DNA form, which is considered here, requires at least 13 water molecules per nucleotide to be stable [87].

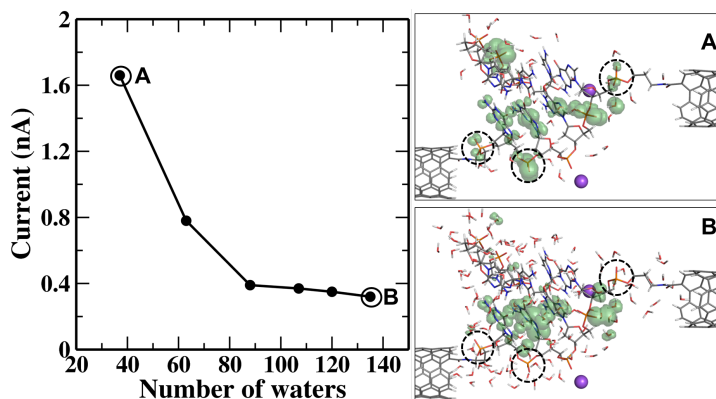


Figure 3.6: Relation between the number of surrounding water molecules and conductivity is shown for 4BP DNA (snapshot 2). Water dipoles generally suppress the conducting state on the negatively charged phosphate groups, leading to reduced conductivity. Including more than 80 water molecules no longer changes the conductivity

We now focus on how the current changes with the number of water molecules around

DNA. This dependence is plotted in Figure 3.6 for snapshot 2. As expected, the current decreases with increased solvation. To understand why, we plot local densities of states for the most dominant transmission peak in the HOMO conduction range for 37 and 135 water molecules. These are shown in Figure 3.6 (A) and (B). Comparing them shows that when the number of waters is increased, charge on the phosphate groups in the DNA backbone is suppressed. This is most likely due to the electrostatic potential of water molecules shifting the energy levels of states localized on the phosphate groups to outside the conductive region. Thus solvent eliminates the CT channel through the DNA backbone leading to decreased conductivity. Our finding agrees with the experimental observations [49] that for a solvated DNA, the charge transfer is not through the sugar-phosphate backbone but through the base pair stack, since the breaks in backbone do not affect CT signal. In the context of studying DNA CT, it is important to include the effects of the first hydration shell, since the existence of the counterions and the water dipoles modulates the local potential and changes the energy levels of the DNA as well as DNA CT.

Effect of DNA conformation

Our calculations show large variations in current between snapshots along the recorded molecular dynamics trajectories. For 4BP DNA, a six orders of magnitude difference between the most and the least conductive snapshots was found. As discussed in previous sections, about two orders of magnitude are due to the effect of counterions and solvent molecules. The remaining variation is due to the DNA configuration itself, as found in the previous section in calculations for dry DNA. It should be noted that in those calculations not only the DNA, but also the linker changes configuration. As found in Section 3.1.1, the linker has negligible effect on the current variation and thus we attribute the variations

Table 3.1: Correlation coefficient of standard helicoidal DNA parameters with current for 10GC DNA.

	mean	minimum	maximum
twist	0.4888	0.1505	-0.0592
roll	0.1571	-0.0128	0.0126
tilt	0.1303	0.181	0.1959
rise	-0.0833	0.2417	0.1569
slide	0.3821	0.383	-0.1662
shift	0.4568	0.6176	0.1275
overlap	0.4208	0.9106	0.051

seen in the dry DNA to the thermally induced structural changes in DNA itself.

CT is found to be sensitive to how the DNA base pairs are dynamically stacked [27, 19, 56, 86]. The double-helix DNA chain exhibits substantial flexibility and CT through DNA has been described by a conformational gating model [64, 66]. Enhanced DNA base motions generally lead to longer-range CT through well-coupled conformations of base domains. Therefore, CT rates have a complicated time dependence due to conformational dynamics. This is consistent with our histogram shown in Figure 3.2(b). However, how do CT-active conformations look like is still elusive. In the following, we analyze the 10BP poly(G)-poly(C) DNA structures recorded in our MD simulations to uncover the key factors that distinguish high and low conductivity configurations. The 20 snapshots of the 10BP DNA (see Figure 3.2(b) for current histogram) are characterized with the standard helicoidal parameters [1], such as rise, twist, roll, tilt, shift, slide and overlap area between the neighboring guanine bases. The parameters are calculated with 3DNA [51]. Using the DNA and the first solvation shell, we analyze correlation between conductivity and the helicoidal parameters. Because these can be calculated for every two consecutive bases

pairs (thus giving us 9 values), we consider correlation with not just average, but also with minimum and maximum values of the parameters. This is shown in Table 3.1, where we find that the dominant factor is the minimum overlap area. This means that DNA conductivity is highly sensitive to its local configuration and that the break between any consecutive base pairs affects the conductivity of the entire molecule. Figure 3.7 shows the plot of the current versus the minimum overlap. A strong correlation between the minimum overlap and conductivity is apparent. Our finding agrees with a previous semiempirical study [82], which found that the effective coupling can increase greatly when by chance the value of many individual couplings is high. They also found that the motion of a purine base parallel to its plane is a critical factor in DNA conductivity.

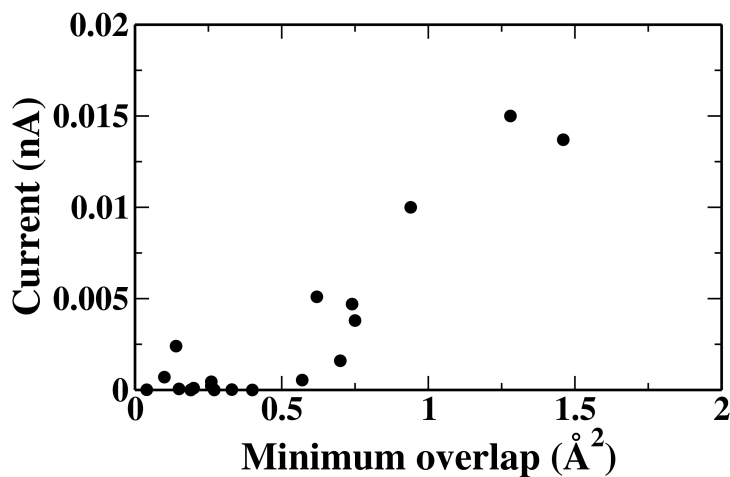


Figure 3.7: Dependence of the conductivity of 10BP poly(G)-poly(C) DNA with the minimum overlap.

In addition to flexible DNA, we also focus on 10BP poly(G)-poly(C) DNA frozen in an optimum B-DNA configuration with only the solvent molecules allowed to move. Quantum transport calculations are carried out for five recorded snapshots. For optimum

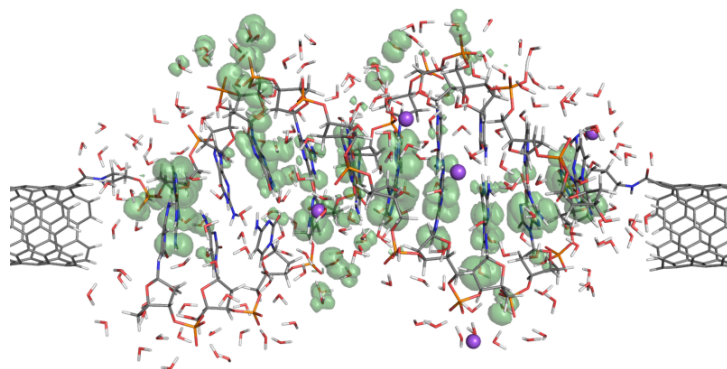


Figure 3.8: Isosurface of the charge density of the most conducting HOMO state from a high conductivity configuration (snapshot 15). This state is extended over most of the guanine bases.

B-DNA, the value of the overlap is 2.23\AA^2 between any two pairs. Note that this is much better than the minimum overlap seen in our MD simulations. In this case, the conductivity is also improved compared to the dynamical DNA structures and we get a current of 0.025 nA, which is nearly 10 times larger than the average current that we have seen in flexible 10BP poly(G)-poly(C) DNA. Thus we conclude that for the poly(G)-poly(C) case the optimum structure is the most conductive conformation.

In order to put the above results into perspective, we analyze the charge distribution

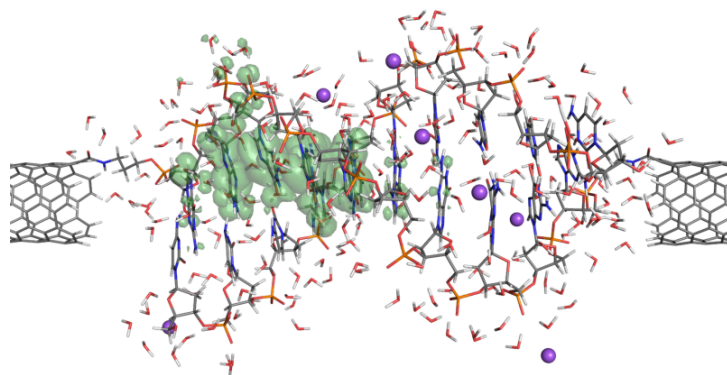


Figure 3.9: Isosurface of charge density of the most conducting state from a poor conducting system (snapshot 16). The charge density is mainly localized on G1-G5.

of the HOMO states. In the case of high conductivity, the HOMO states are generally delocalized over the guanine bases. Figure 3.8 shows a HOMO state for a representative high conductivity configuration (snapshot 15). For the low conductivity configurations, the HOMO states are no longer extended, because the π -stacking is jeopardized due to the small overlaps, as shown in Figure 3.9. In this snapshot, the HOMO states are localized on a few guanine bases. As a result, the calculated current is very small.

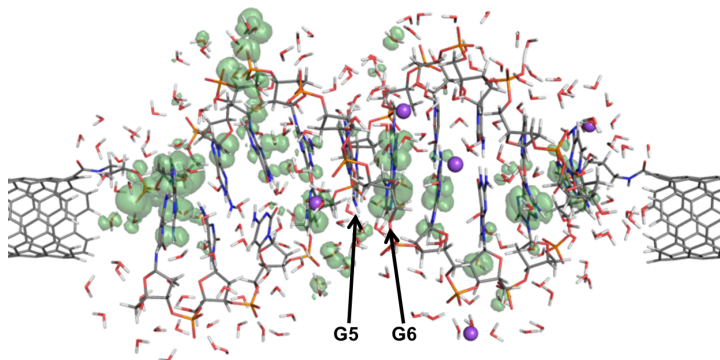


Figure 3.10: The charge delocalization of the most conducting state across G5 and G6 is reduced due to smaller minimum overlap between G5 and G6.

To further investigate the overlap effect, we start with a highly conductive configuration (snapshot 15, the minimum overlap is between G5 and G6) and run a constrained MD simulation in which only a single base pair (G6-C6) is allowed to move while the rest of the system is frozen. The motivation is to examine the conductivity change as the minimum overlap changes with the thermal motion of the G6-C6 pair. From our restrained MD simulation, we extract a frame with the lowest minimum overlap value, which corresponds to the case in which the overlap between G5 and G6 decreases from 1.46\AA^2 to 0.73\AA^2 while that between G6 and G7 stays mostly unchanged. The most conducting state for this configuration is shown in Figure 3.10. As one can see, the conductive state

Table 3.2: Correlation coefficient of standard helicoidal parameters with current for 10AT DNA

	mean	minimum	maximum
twist	-0.2009	-0.1178	-0.1027
roll	-0.1915	-0.2666	-0.08
tilt	-0.2392	0.0184	-0.1494
rise	0.3082	0.1626	-0.0373
slide	-0.0674	-0.1361	-0.2459
shift	0.0935	0.1678	-0.0507
overlap	-0.0456	0.3781	-0.2635

becomes substantially less extended in the entire molecule when the minimum overlap is reduced. This phenomenon is confirmed for the other HOMO states near the Fermi level. The current calculated from the snapshot with reduced minimum overlap is smaller by a factor of three. We conclude that the overlaps between the neighbor guanine bases, especially the minimum overlaps, are critical in determining the degree of delocalization, which in turn dictates conductivity.

We also investigate 10BP poly(A)-poly(T) DNA in the same manner as 10BP poly(G)-poly(C) DNA. There are important differences between poly(G)-poly(C) and poly(A)-poly(T) chains. First, an A-T pair has only two hydrogen bonds compared to three for G-C, which makes the poly(A)-poly(T) more flexible under thermal motion. Furthermore, the overlaps between AT pairs are smaller compared to GC pairs (the average minimum overlap is 0.4\AA^2 for poly(A)-poly(T) and 0.75\AA^2 for poly(G)-poly(C)). In addition, the HOMO energy of A is lower than that of G. This could lead to a larger gap between HOMO states and Fermi level of the leads. However, water states in the gap may randomly create CT channels through water molecules as shown in Figure 3.11. Correlation between

poly(A)-poly(T) DNA parameters is shown in Table 3.2. While the minimum overlap is still the best parameter governing the conductance, the correlation is much smaller compared to the poly(G)-poly(C) case.

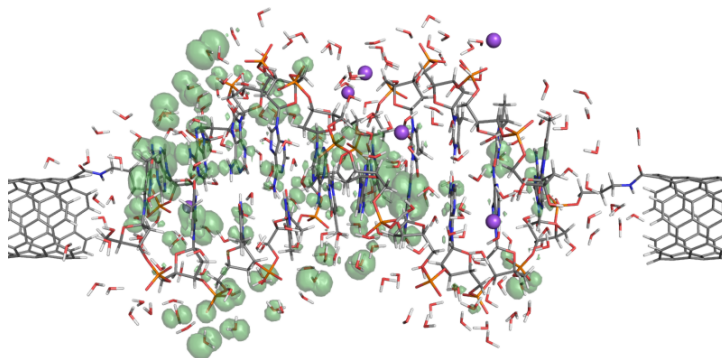


Figure 3.11: Isosurface of charge distribution of a conducting state. State occupies water molecules in a 10BP poly(A)-poly(T) DNA

Another difference between the poly(A)-poly(T) and poly(G)-poly(C) chains is that for the former, the ideal B-DNA conformation does not yield much better conductance than the dynamic structures sampled from our MD calculation. Specifically, the current through the ideal conformation is 0.0035 nA on average, while it is 0.0028 nA on average for the flexible sampled conformations.

3.3.2 DNA sequence effect

Experiments have shown that DNA sequence also plays a role in DNA charge transport, and that a mismatched base pair reduces the conductivity [41, 26, 80]. Here we study how DNA conductivity changes when a single base pair in a homogeneous 10BP poly(G)-poly(C) DNA is replaced with AT(matched), GT or AC at position 6. The DNA structures are built by 3-DNA software [51] and relaxed in the CHARMM force field.

Table 3.3: Calculated current (nA) for different flexible sequences

	GC	AT	GT	AC
Average	0.0029	0.0021	0.0028	0.0033

For each sequence, we extract 10 snapshots from the 2 ns MD simulations. The average currents of these snapshots are similar with those flexible poly(G)-poly(C) DNA, as shown in Table 3.3. To exclude the effect of conformational fluctuations we repeat this calculation with the DNA structures frozen in an ideal B-DNA configurations with only the solvent allowed to move to obtain a good description of the DNA environment. For each case, quantum transport calculations are carried out for five recorded snapshots. The results for different sequences are summarized in Table 3.4. Note that in this case significant differences are observed between the four cases.

For the ideal poly(G)-poly(C) DNA, the conducting states are delocalized as shown in Figure 3.12. This is expected due to the large coupling between neighboring guanine bases in ideal DNA structures. In this case, good conductivity can be achieved because all the overlaps are equally large and the states are delocalized. As we can see from Table 3.4, the conductivity in ideal 10BP poly(G)-poly(C) DNA is relatively large. However, the signal decreases by a factor of five upon an insertion of a base pair different from GC. This indicates that the homogeneous sequence is essential for efficient coherent transport along DNA. A single non-GC base pair can destroy the HOMO alignment. As a result, the HOMO states, main contributors to the current, are no longer extended on site 6. This is shown in Figure 3.13 for the case of a mismatched GT substituted in position 6. Note the charge contraction near site 6, which could lead to backscattering

Table 3.4: Calculated current (nA) for different sequences at site 6

	GC	AT	GT	AC
Average	0.0252	0.0058	0.0046	0.0048
Max	0.0400	0.0070	0.0061	0.0069
Min	0.0150	0.0040	0.0025	0.0032

[76]. Similar phenomena are also found for the AT and AC base pair insertions. The inserted base pair, regardless of its identity, substantially decreases CT compared to the homogeneous sequence. A non-homogeneous base pair incorporated into a poly(G)-poly(C) domain acts like a tunneling barrier and thus reduces the charge delocalization as well as charge transport. This is consistent with previous first-principle calculations which showed that even the very modest sequence variation in poly(G)-poly(C) sequence lead to electron localization which limits the coherent transport mechanism [13, 55]. The sequence inhomogeneities are expected to change the onsite energy and the base-base coupling and therefore jeopardize the natural pathway for charge transport through

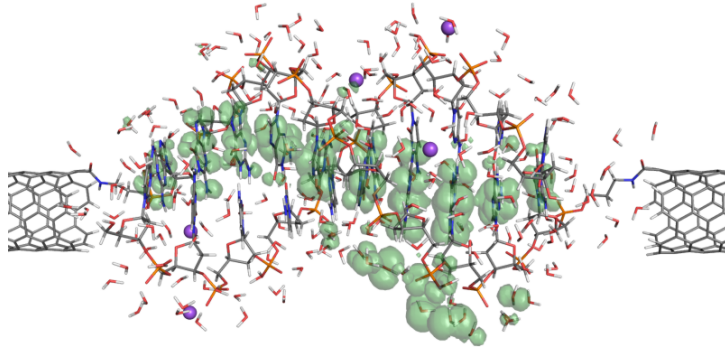


Figure 3.12: Isosurface of the charge density of the most conducting level from an optimum 10BP DNA system. The charge density of this level is uniformly delocalized through the entire system.

guanine bases.

O'Neill and Barton examined the temperature dependence of the yield of CT between photoexcited 2-aminopurine and G through DNA bridges of varied length and sequence [64]. They found that the yield of CT through mixed or mismatched sequence bridge is not as efficacious at a low temperature as the well-coupled homogeneous sequence. The influence of temperature on CT is so dramatic that CT yields through a mixed or mismatched sequence approaches the yield of a homogeneous bridge at high temperature before DNA melting. Based on our calculations, we also find that a single inserted different base pair in homogeneous DNA decrease CT by a factor of five in relaxed optimum DNA structures, this corresponds to low temperature limit in experiment. Our calculated results qualitatively agree with the experiments [65, 64, 89], which showed that the sequence variation in a homogeneous DNA chain reduces CT signal only at lower temperature, but the sequence effect diminishes as temperature increases.

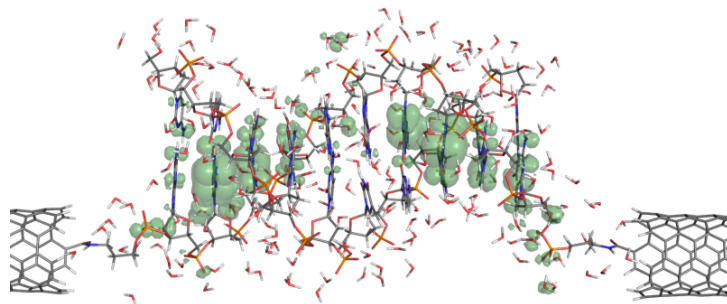


Figure 3.13: Isosurface of charge density of the most conducting state from 10BP DNA with a GT mismatched base pair at site 6. Notice the contraction of charge distribution at site 5 and 6. Counterions are not shown for simplicity.

3.4 Conclusions and summary

In this work, we investigated conductivity of B-DNA using *ab initio* calculations. For the first time, we considered multiple DNA conformations sampled from MD simulations. We found that thermal fluctuations cause large variations of the current. The best predictor of good conductivity is the overlap area between neighboring base pairs.

From our calculations, we favor the mechanism of single-step coherent transport determined by charge delocalization over the superexchange and the hopping model. The decay parameter of electronic conductance is found to be $\beta = 0.18\text{\AA}^{-1}$ by comparing the snapshot-averaged conductivity from the two different length homogeneous DNA systems. This small decay parameter indicates that DNA could be a very promising conductor. If charge transport is dominated by superexchange, one would expect the falloff parameter to be much larger, e.g., $\beta = 1.0\text{\AA}^{-1}$ [75]. Moreover, in the well-conducting DNA where all overlaps between the neighbor guanine bases are large, extended conducting states can be formed. The charge delocalization again indicates that superexchange tunneling model in which intervening bases are not occupied does not make a major contribution to the mechanism of CT in DNA. The hopping model in which the charge is localized is also excluded here. Our results underscore the importance of coherent steps in DNA-mediated CT process. Barton and co-workers already proposed a coherent single step mechanism dependent upon transient delocalized domains [20]. In their experiment, they separated the single step process CT with the multi-step process CT and found that the single-step coherent CT overtakes the incoherent CT, and plays a dominant role in 10 BP DNA. From our results, the extended coherent states are transient depending on the possibility of achieving good stacking for every pair of the neighboring guanine bases simultaneously, since the minimum overlaps along the chain determine the conductivity.

Finally, we discovered that different base pairs inserted into the homogeneous sequence act like a tunneling barrier and thus reduce the conductivity significantly. Our results indicate that the sensing of sequence variation will be most selective at low temperatures. These results provide insight for fundamental parameters governing DNA CT in a homogeneous sequence and sensing applications in modified DNA sequence under biologically relevant conditions.

REFERENCES

- [1] Definitions and nomenclature of nucleic acid structure parameters. *EMBO J.*, 8(1):1–4, January 1989. PMID: 2714249.
- [2] Robert N. Barnett, Charles L. Cleveland, Abraham Joy, Uzi Landman, and Gary B. Schuster. Charge migration in DNA: ion-gated transport. *Science*, 294(5542):567–571, October 2001.
- [3] Yuri A. Berlin, Alexander L. Burin, and Mark A. Ratner. On the long-range charge transfer in DNA. *J. Phys. Chem. A*, 104(3):443–445, January 2000.
- [4] J. Bernholc, M. Hodak, and W. Lu. Recent developments and applications of the real-space multigrid method. *J Phys Condens Matter*, 20(29):294205–294205, 2008.
- [5] M. Bixon, Bernd Giese, Stephan Wessely, Thomas Langenbacher, Maria E. Michel-Beyerle, and Joshua Jortner. Long-range charge hopping in DNA. *PNAS*, 96(21):11713–11716, October 1999. PMID: 10518515.
- [6] Elizabeth M. Boon, Alison L. Livingston, Nikolas H. Chmiel, Sheila S. David, and Jacqueline K. Barton. DNA-mediated charge transport for DNA repair. *Proceedings of the National Academy of Sciences of the United States of America*, 100(22):12543–12547, October 2003.
- [7] M. Brandbyge, J. L. Mozos, P. Ordejón, J. Taylor, and K. Stokbro. Density-functional method for nonequilibrium electron transport. *Physical Review B*, 65(16), 2002.

- [8] Erez Braun, Yoav Eichen, Uri Sivan, and Gdalyahu Ben-Yoseph. DNA-templated assembly and electrode attachment of a conducting silver wire. *Nature*, 391(6669):775–778, February 1998.
- [9] E. L. Briggs, D. J. Sullivan, and J. Bernholc. Real-space multigrid-based approach to large-scale electronic structure calculations. *Phys. Rev. B*, 54(20):14362–14375, 1996.
- [10] Junghuei Chen and Nadrian C. Seeman. Synthesis from DNA of a molecule with the connectivity of a cube. *Nature*, 350(6319):631–633, April 1991.
- [11] Hezy Cohen, Claude Nogues, Ron Naaman, and Danny Porath. Direct measurement of electrical transport through single DNA molecules of complex sequence. *Proceedings of the National Academy of Sciences of the United States of America*, 102(33):11589–11593, 2005.
- [12] Peter J. Dandliker, R. Erik Holmlin, and Jacqueline K. Barton. Oxidative thymine dimer repair in the DNA helix. *Science*, 275(5305):1465–1468, March 1997.
- [13] P. J. de Pablo, F. Moreno-Herrero, J. Colchero, J. Gmez Herrero, P. Herrero, A. M. Bar, Pablo Ordejón, Jos M. Soler, and Emilio Artacho. Absence of dc-conductivity in -DNA. *Phys. Rev. Lett.*, 85(23):4992–4995, December 2000.
- [14] P. A. M. Dirac. On the theory of quantum mechanics. *Proceedings of the Royal Society of London. Series A, Containing Papers of a Mathematical and Physical Character*, 112(762):661–677, October 1926. ArticleType: research-article / Full publication date: Oct. 1, 1926 / Copyright 1926 The Royal Society.

- [15] Benjamin Elias, Fangwei Shao, and Jacqueline K. Barton. Charge migration along the DNA duplex: hole versus electron transport. *J. Am. Chem. Soc.*, 130(4):1152–1153, January 2008.
- [16] J. L. Fattebert and J. Bernholc. Towards grid-based o (n) density-functional theory methods: Optimized nonorthogonal orbitals and multigrid acceleration. *Phys. Rev. B*, 62(3):1713–1722, 2000.
- [17] S. E. Feller and A. D. MacKerell. An improved empirical potential energy function for molecular simulations of phospholipids. *J Phys Chem A*, 104(31):7510–7515, 2000.
- [18] Nicolas Foloppe and Alexander D. MacKerell, Jr. All-atom empirical force field for nucleic acids: I. parameter optimization based on small molecule and condensed phase macromolecular target data. *Journal of Computational Chemistry*, 21(2):86104, 2000.
- [19] Joseph C. Genereux and Jacqueline K. Barton. Mechanisms for DNA charge transport. *Chem. Rev.*, 110(3):1642–1662, March 2010.
- [20] Joseph C. Genereux, Stephanie M. Wuerth, and Jacqueline K. Barton. Single-step charge transport through DNA over long distances. *J. Am. Chem. Soc.*, 133(11):3863–3868, March 2011.
- [21] Bernd Giese. Long-distance charge transport in DNA: the hopping mechanism. *Acc. Chem. Res.*, 33(9):631–636, September 2000.

- [22] Bernd Giese, Jérôme Amaudrut, Anne-Kathrin Khler, Martin Spormann, and Stephan Wessely. Direct observation of hole transfer through DNA by hopping between adenine bases and by tunnelling. *Nature*, 412(6844):318–320, July 2001.
- [23] Ferdinand C. Grozema, Yuri A. Berlin, and Laurens D. A. Siebbeles. Mechanism of charge migration through DNA: molecular wire behavior, single-step tunneling or hopping? *J. Am. Chem. Soc.*, 122(44):10903–10909, November 2000.
- [24] Ferdinand C. Grozema, Stefano Tonzani, Yuri A. Berlin, George C. Schatz, Laurens D. A. Siebbeles, and Mark A. Ratner. Effect of structural dynamics on charge transfer in DNA hairpins. *Journal of the American Chemical Society*, 130(15):5157–5166, April 2008.
- [25] Ferdinand C. Grozema, Stefano Tonzani, Yuri A. Berlin, George C. Schatz, Laurens D. A. Siebbeles, and Mark A. Ratner. Effect of structural dynamics on charge transfer in DNA hairpins. *J. Am. Chem. Soc.*, 130(15):5157–5166, April 2008.
- [26] Xuefeng Guo, Alon A. Gorodetsky, James Hone, Jacqueline K. Barton, and Colin Nuckolls. Conductivity of a single DNA duplex bridging a carbon nanotube gap. *Nat Nano*, 3(3):163–167, March 2008.
- [27] Daniel B. Hall and Jacqueline K. Barton. Sensitivity of DNA-Mediated electron transfer to the intervening π -stack: a probe for the integrity of the DNA base stack. *J. Am. Chem. Soc.*, 119(21):5045–5046, May 1997.
- [28] Daniel B. Hall, R. Erik Holmlin, and Jacqueline K. Barton. Oxidative DNA damage through long-range electron transfer. *Nature*, 382(6593):731–735, August 1996.

- [29] D. R. Hamann, M. Schlter, and C. Chiang. Norm-conserving pseudopotentials. *Phys. Rev. Lett.*, 43(20):1494, November 1979. Copyright (C) 2009 The American Physical Society; Please report any problems to prola@aps.org.
- [30] Elizabeth Hatcher, Alexander Balaeff, Shahar Keinan, Ravindra Venkatramani, and David N. Beratan. PNA versus DNA: effects of structural fluctuations on electronic structure and hole-transport mechanisms. *J. Am. Chem. Soc.*, 130(35):11752–11761, September 2008.
- [31] E. Hernandez and M. J. Gillan. Self-consistent first-principles technique with linear scaling. *Phys. Rev. B*, 51(15):10157–10160, April 1995.
- [32] E. Hernandez, M. J. Gillan, and C. M. Goringe. Linear-scaling density-functional-theory technique: The density-matrix approach. *Phys. Rev. B*, 53(11):7147–7157, March 1996.
- [33] Conyers Herring. A new method for calculating wave functions in crystals. *Phys. Rev.*, 57(12):1169–1177, June 1940.
- [34] Conyers Herring and A. G. Hill. The theoretical constitution of metallic beryllium. *Phys. Rev.*, 58(2):132–162, July 1940.
- [35] Joshua Hihath, Bingqian Xu, Peiming Zhang, and Nongjian Tao. Study of single-nucleotide polymorphisms by means of electrical conductance measurements. *Proceedings of the National Academy of Sciences of the United States of America*, 102(47):16979–16983, November 2005.

- [36] Miroslav Hodak, Shuchun Wang, Wenchang Lu, and J. Bernholc. Implementation of ultrasoft pseudopotentials in large-scale grid-based electronic structure calculations. *Phys. Rev. B*, 76(8):085108–8, 2007.
- [37] Takeo Hoshi and Takeo Fujiwara. Fully-selfconsistent electronic-structure calculation \ using nonorthogonal localized orbitals within a finite-difference \ real-space scheme and ultrasoft pseudopotential. *Journal of the Physical Society of Japan*, 66(12):3710–3713, 1997.
- [38] Joshua Jortner, Mordechai Bixon, Thomas Langenbacher, and Maria E. Michel-Beyerle. Charge transfer and transport in DNA. *PNAS*, 95(22):12759–12765, October 1998. PMID: 9788986.
- [39] A. Yu. Kasumov. Proximity-induced superconductivity in DNA. *Science*, 291(5502):280–282, January 2001.
- [40] Chao-Cheng Kaun and Hong Guo. Resistance of alkanethiol molecular wires. *Nano Lett.*, 3(11):1521–1525, November 2003.
- [41] Shana O. Kelley and Jacqueline K. Barton. Electron transfer between bases in double helical DNA. *Science*, 283(5400):375–381, January 1999. PMID: 9888851.
- [42] Shana O. Kelley, R. Erik Holmlin, Eric D. A. Stemp, and Jacqueline K. Barton. Photoinduced electron transfer in ethidium-modified DNA duplexes: dependence on distance and base stacking. *J. Am. Chem. Soc.*, 119(41):9861–9870, October 1997.
- [43] Shana O. Kelley, Nicole M. Jackson, Michael G. Hill, and Jacqueline K. Barton. Long-range electron transfer through DNA films. *Angewandte Chemie International Edition*, 38(7):941945, 1999.

- [44] Heeyoung Kim, One Choi, and Eunji Sim. Pathway analysis on DNA charge transfer through adenine and guanine bridges. *J. Phys. Chem. C*, 114(48):20394–20400, December 2010.
- [45] Leonard Kleinman and D. M. Bylander. Efficacious form for model pseudopotentials. *Phys. Rev. Lett.*, 48(20):1425, 1982. Copyright (C) 2009 The American Physical Society; Please report any problems to prola@aps.org.
- [46] I. V. Kurnikov, G. S. M. Tong, M. Madrid, and D. N. Beratan. Hole size and energetics in double helical DNA: competition between quantum delocalization and solvation localization. *J. Phys. Chem. B*, 106(1):7–10, January 2002.
- [47] M. H. Lee, S. Avdoshenko, R. Gutierrez, and G. Cuniberti. Charge migration through DNA molecules in the presence of mismatches. *Phys. Rev. B*, 82(15):155455, October 2010.
- [48] Frederick D Lewis, Huihe Zhu, Pierre Daublain, Karsten Sigmund, Torsten Fiebig, Milen Raytchev, Qiang Wang, and Vladimir Shafirovich. Getting to guanine: mechanism and dynamics of charge separation and charge recombination in DNA revisited. *Photochem. Photobiol. Sci.*, 7(5):534–539, May 2008. PMID: 18465008.
- [49] Tao Liu and Jacqueline K. Barton. DNA electrochemistry through the base pairs not the SugarPhosphate backbone. *J. Am. Chem. Soc.*, 127(29):10160–10161, July 2005.
- [50] Wenchang Lu, Vincent Meunier, and J. Bernholc. Nonequilibrium quantum transport properties of organic molecules on silicon. *Phys. Rev. Lett.*, 95(20):206805, November 2005.

- [51] Xiang-Jun Lu and Wilma K. Olson. 3DNA: a software package for the analysis, rebuilding and visualization of threedimensional nucleic acid structures. *Nucl. Acids Res.*, 31(17):5108–5121, September 2003. PMID: 12930962.
- [52] A. D. MacKerell, D. Bashford, Bellott, R. L. Dunbrack, J. D. Evanseck, M. J. Field, S. Fischer, J. Gao, H. Guo, S. Ha, D. Joseph-McCarthy, L. Kuchnir, K. Kuczera, F. T. K. Lau, C. Mattos, S. Michnick, T. Ngo, D. T. Nguyen, B. Prodhom, W. E. Reiher, B. Roux, M. Schlenkrich, J. C. Smith, R. Stote, J. Straub, M. Watanabe, J. Wirkiewicz-Kuczera, D. Yin, and M. Karplus. All-atom empirical potential for molecular modeling and dynamics studies of proteins. *J. Phys. Chem. B*, 102(18):3586–3616, April 1998.
- [53] Alexander D. MacKerell and Nilesh K. Banavali. All-atom empirical force field for nucleic acids: II. application to molecular dynamics simulations of DNA and RNA in solution. *Journal of Computational Chemistry*, 21(2):105120, 2000.
- [54] Yaku Maeda, Akisumi Okamoto, Yasuhiro Hoshihara, Takayuki Tsukamoto, Yasuyuki Ishikawa, and Noriyuki Kurita. Effect of hydration on electrical conductivity of DNA duplex: Greens function study combined with DFT. *Computational Materials Science*, 53(1):314–320, February 2012.
- [55] Sairam S. Mallajosyula, J. C. Lin, D. L. Cox, S. K. Pati, and R. R. P. Singh. Sequence dependent electron transport in wet DNA: abinitio and molecular dynamics studies. *Phys. Rev. Lett.*, 101(17):176805, October 2008.
- [56] Sairam S. Mallajosyula and Swapan K. Pati. Toward DNA conductivity: A theoretical perspective. *J. Phys. Chem. Lett.*, 1(12):1881–1894, June 2010.

- [57] Andrew Marshall and John Hodgson. DNA chips: An array of possibilities. *Nature Biotechnology*, 16(1):27–31, January 1998.
- [58] Eric Meggers, Maria E. Michel-Beyerle, and Bernd Giese. Sequence dependent long range hole transport in DNA. *J. Am. Chem. Soc.*, 120(49):12950–12955, December 1998.
- [59] CJ Murphy, MR Arkin, Y Jenkins, ND Ghatlia, SH Bossmann, NJ Turro, and JK Barton. Long-range photoinduced electron transfer through a DNA helix. *Science*, 262(5136):1025–1029, November 1993.
- [60] Marco Buongiorno Nardelli, J. L. Fattebert, and J. Bernholc. O(n) real-space method for ab initio quantum transport calculations: Application to carbon nanotube-metal contacts. *Physical Review B*, 64(24):245423, 2001.
- [61] H. Ness, S. A. Shevlin, and A. J. Fisher. Coherent electron-phonon coupling and polaronlike transport in molecular wires. *Phys. Rev. B*, 63(12):125422, March 2001.
- [62] R. W. Nunes and David Vanderbilt. Generalization of the density-matrix method to a nonorthogonal basis. *Phys. Rev. B*, 50(23):17611–17614, December 1994.
- [63] Akimitsu Okamoto, Kazuo Tanaka, and Isao Saito. Rational design of a DNA wire possessing an extremely high hole transport ability. *J. Am. Chem. Soc.*, 125(17):5066–5071, April 2003. PMID: 12708856.
- [64] Melanie A. O’Neil and Jacqueline K. Barton. DNA charge transport: conformationally gated hopping through stacked domains. *J. Am. Chem. Soc.*, 126(37):11471–11483, September 2004.

- [65] Melanie A. O’Neill, Hans-Christian Becker, Chaozhi Wan, Jacqueline K. Barton, and Ahmed H. Zewail. Ultrafast dynamics in DNA-Mediated electron transfer: Base gating and the role of temperature. *Angewandte Chemie*, 115(47):60766080, 2003.
- [66] Melanie A. O’Neill and Jacqueline K. Barton. DNA-Mediated charge transport requires conformational motion of the DNA bases: elimination of charge transport in rigid glasses at 77 k. *J. Am. Chem. Soc.*, 126(41):13234–13235, October 2004.
- [67] C. D. Pemmaraju, I. Rungger, X. Chen, A. R. Rocha, and S. Sanvito. Ab initio study of electron transport in dry poly(g)-poly(c) a-DNA strands. *Phys. Rev. B*, 82(12):125426, September 2010.
- [68] J. P. Perdew. Generalized gradient approximation for the fermion kinetic energy as a functional of the density. *Phys. Lett. A*, 165(1):79–82, 1992.
- [69] John P. Perdew, Kieron Burke, and Matthias Ernzerhof. Generalized gradient approximation made simple. *Phys. Rev. Lett.*, 77(18):3865, 1996.
- [70] James C. Phillips, Rosemary Braun, Wei Wang, James Gumbart, Emad Tajkhorshid, Elizabeth Villa, Christophe Chipot, Robert D. Skeel, Laxmikant Kal, and Klaus Schulten. Scalable molecular dynamics with NAMD. *J. Comput. Chem.*, 26(16):17811802, 2005. PMC2486339.
- [71] James C. Phillips and Leonard Kleinman. New method for calculating wave functions in crystals and molecules. *Phys. Rev.*, 116(2):287, October 1959. Copyright (C) 2009 The American Physical Society; Please report any problems to prola@aps.org.

- [72] Danny Porath, Alexey Bezryadin, Simon de Vries, and Cees Dekker. Direct measurement of electrical transport through DNA molecules. *Nature*, 403(6770):635–638, February 2000.
- [73] Danny Porath, Gianaurelio Cuniberti, and Rosa Di Felice. Charge transport in DNA-Based devices. In G.B. Schuster, editor, *Long-Range Charge Transfer in DNA II*, volume 237 of *Topics in Current Chemistry*, pages 183–228. Springer Berlin / Heidelberg, 2004.
- [74] A. Rakitin, P. Aich, C. Papadopoulos, Yu. Kobzar, A. S. Vedeneev, J. S. Lee, and J. M. Xu. Metallic conduction through engineered DNA: DNA nanoelectronic building blocks. *Phys. Rev. Lett.*, 86(16):3670–3673, April 2001.
- [75] Nicolas Renaud, Yuri A. Berlin, Frederick D. Lewis, and Mark A. Ratner. Between superexchange and hopping: An intermediate charge-transfer mechanism in poly(a)-poly(t) DNA hairpins. *J. Am. Chem. Soc.*, 135(10):3953–3963, March 2013.
- [76] Stephan Roche. Sequence dependent DNA-Mediated conduction. *Phys. Rev. Lett.*, 91(10):108101, September 2003.
- [77] Frisco Rose, Miroslav Hodak, and Jerzy Bernholc. Mechanism of copper(II)-induced misfolding of parkinson’s disease protein. *Sci. Rep.*, 1, June 2011.
- [78] Siegmur Roth and David Carroll. *One-dimensional metals*. Wiley. com, 2004.
- [79] M. P. Lopez Sancho, J. M. Lopez Sancho, and J. Rubio. Quick iterative scheme for the calculation of transfer matrices: application to mo (100). *J. Phys. F: Met. Phys.*, 14(5):1205, May 1984.

- [80] Jason D. Slinker, Natalie B. Muren, Sara E. Renfrew, and Jacqueline K. Barton. DNA charge transport over 34 nm. *Nat Chem*, 3(3):228–233, March 2011.
- [81] Christopher R. Treadway, Michael G. Hill, and Jacqueline K. Barton. Charge transport through a molecular [pi]-stack: double helical DNA. *Chemical Physics*, 281(2-3):409–428, August 2002.
- [82] Alessandro Troisi and Giorgio Orlandi. Hole migration in DNA: a theoretical analysis of the role of structural fluctuations. *J. Phys. Chem. B*, 106(8):2093–2101, February 2002.
- [83] D. Vanderbilt. Soft self-consistent pseudopotentials in a generalized eigenvalue formalism. *Phys. Rev. B*, 41(11):7892–7895, 1990.
- [84] David Vanderbilt. Soft self-consistent pseudopotentials in a generalized eigenvalue formalism. *Physical Review B*, 41(11):7892, 1990.
- [85] Josh Vura-Weis, Michael R Wasielewski, Arun K Thazhathveetil, and Frederick D Lewis. Efficient charge transport in DNA diblock oligomers. *J. Am. Chem. Soc.*, 131(28):9722–9727, July 2009. PMID: 19558185.
- [86] Hans-Achim Wagenknecht. Electron transfer processes in DNA: mechanisms, biological relevance and applications in DNA analytics. *Nat. Prod. Rep.*, 23(6):973–1006, November 2006.
- [87] John M. Warman, Matthijs P. de Haas, and Allan Rupprecht. DNA: a molecular wire? *Chemical Physics Letters*, 249(56):319–322, February 1996.
- [88] A. R. Williams, Peter J. Feibelman, and N. D. Lang. Green’s-function methods for electronic-structure calculations. *Phys. Rev. B*, 26(10):5433–5444, November 1982.

- [89] Chris H. Wohlgamuth, Marc A. McWilliams, and Jason D. Slinker. Temperature dependence of electrochemical DNA charge transport: Influence of a mismatch. *Anal. Chem.*, 85(3):1462–1467, February 2013.
- [90] Xu, Zhang, Li, and Tao. Direct conductance measurement of single DNA molecules in aqueous solution. *Nano Letters*, 4(6):1105–1108, June 2004.
- [91] K.-H. Yoo, D. H. Ha, J.-O. Lee, J. W. Park, Jinhee Kim, J. J. Kim, H.-Y. Lee, T. Kawai, and Han Yong Choi. Electrical conduction through poly(dA)-Poly(dT) and poly(dG)-Poly(dC) DNA molecules. *Phys. Rev. Lett.*, 87(19):198102, October 2001.
- [92] Y. Zhang, R. H. Austin, J. Kraeft, E. C. Cox, and N. P. Ong. Insulating behavior of -DNA on the micron scale. *Phys. Rev. Lett.*, 89(19):198102, October 2002.

APPENDIX

Appendix A

Computational technique

A.1 Adaptive integration

The transmission curves obtained from quantum calculations usually contain very sharp peaks [67, 55]. In order to calculate the current accurately, we have implemented a simple adaptive algorithm in energy integration. At first, we calculate the transmission at uniformly distributed energy points near the Fermi level. Then we locate the peaks in the transmission and insert energy points near the peak with energy spacing being half of the previous level. The procedure is iterated until we obtain a converged current. One example of snapshot 2 in 4BP calculation is shown in Figure A.1. The calculated current is converged to 0.37 nA with the finest energy spacing of about 10^{-6} eV (level 11).

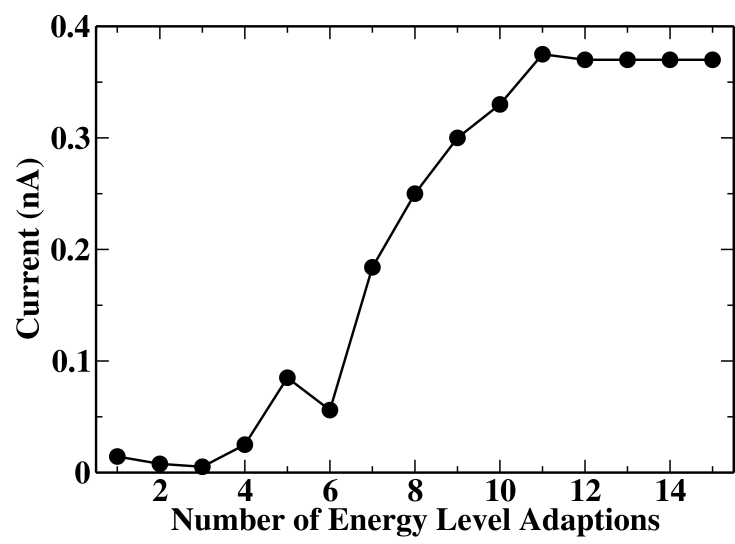


Figure A.1